UNIVERSIDAD NACIONAL AUTÓNOMA DE MÉXICO
PROGRAMA DE MAESTRÍA Y DOCTORADO EN INGENIERÍA
INGENIERÍA MECÁNICA – TERMOFLUIDOS

CARACTERIZACIÓN HIDRODINÁMICA DE FLUJOS MULTIFÁSICOS EN
TANQUES AGITADOS

TESIS
QUE PARA OPTAR POR EL GRADO DE:
DOCTOR EN INGENIERÍA

PRESENTA:

FABIO ERNESTO MANCILLA RAMOS

TUTOR PRINCIPAL:

GABRIEL ASCANIO GASCA, CCADET

COMITÉ TUTOR:

FRANCISCO SOLORIO ORDAZ, FI
ROBERTO ZENIT CAMACHO, IIM

MÉXICO, D. F. FEBRERO, 2015

JURADO ASIGNADO:

Presidente: DR. EDUARDO RAMOS MORA

Secretario: DR. FRANCISCO SOLORIO ORDAZ

Vocal: DR. GABRIEL ASCANIO GASCA

1 er. Suplente: DR. ROBERTO ZENIT CAMACHO

2 do. Suplente: DR. MARTÍN SALINAS VÁZQUEZ

Lugares donde se realizó la tesis:

INSTITUTO DE INVESTIGACIONES EN MATERIALES, UNAM, MÉXICO.
GRUPO DE FÍSICA DE FLUIDOS, UNIVERSIDAD DE TWENTE, HOLANDA.

TUTOR DE TESIS:

GABRIEL ASCANIO GASCA

FIRMA

Caracterización Hidrodinámica de Flujos Multifásicos en Tanques Agitados (Bubbles in Turbulence)

Ernesto Mancilla

February 5, 2015

Contents

Resumen

La turbulencia aparece frecuentemente en la naturaleza y en diversos procesos industriales. A pesar de que la mecánica involucrada en los flujos turbulentos ha sido estudiada extensivamente, aún existen una serie de aspectos que no han sido comprendidos en su totalidad. Cuando la turbulencia es asociada a los flujos multifásicos, este fenómeno se vuelve aun más complejo. Es necesario realizar más estudios para entender los mecanismos físicos que describen la interacción entre flujos turbulentos y partículas. El principal objetivo de este trabajo es obtener algún conocimiento de los mecanismos físicos involucrados en flujos turbulentos multifásicos. Con este propósito se estudiaron diversos casos, pero con objetivos relacionados, en los que la interacción de burbujas y campos turbulentos conocidos es analizada. En este trabajo se presenta la interacción de flujos turbulentos con burbujas individuales y también los casos en los cuales se tiene una alta concentración de ellas. Primeramente se presenta aquí la caracterización y el cambio que se genera en un tanque agitado mecánicamente debido a la adición de burbujas, esto nos permite observar la importancia que tienen las condiciones de inyección de gas en este tipo de sistemas. Más adelante se muestra el comportamiento que se presenta al introducir burbujas en una campo isotrópico turbulento y como estas pueden no solo verse influenciadas por el campo sino también cómo pueden modificar la disipacin de energía turbulenta, lo cual que ha encontrado es función del tamao de burbuja, la fracción de gas suministrada, entre otros parámetros. Finalmente se analiza el caso en el cual las burbujas sufren una deformación extrema y las condiciones para las cuales puede presentarse incluso la ruptura, encontrándose como estos casos pueden describirse por medio del análisis del campo turbulento a su alrededor. La tesis está estructurada de esta manera para facilitar el análisis de los tanques agitados aislando los efectos que se tienen, simplificando la ge-

ometría y considerando una turbulencia homogénea. Además de que de esta manera se puede observar claramente la influencia que el flujo turbulento tiene sobre las burbujas ya sean estas una sola o cúmulos de ellas.

Abstract

Turbulence is commonly found in nature and in many industrial processes. In spite that the mechanics of turbulent flows have been extensively studied, several issues are not completely understood. When the turbulence is associated to a multiphase flow, the phenomena becomes more complex. Further studies are needed to completely understand the physical mechanisms describing the interaction of turbulent flows and particles. The principal objective of this work is to provide some insights about the main physical mechanisms involved in multiphase turbulent flows. For this purpose, different but related experiments were studied. In this work the interaction of turbulence and single and multiple bubbles at a high concentration are presented. Firstly the characterization and change generated in a mechanical stirred tank due to the addition of bubbles is presented. This study allows us to observe the importance of gas injection conditions in such systems. Subsequently the behavior of bubbles in an isotropic turbulent field is investigated. Not only the bubbles can be influenced by the flow, the bubbles can also modify the turbulent energy dissipation. This process depends on the bubble size, gas fraction, among others. Finally, the case in which the bubbles suffer a large deformation is analyzed; the conditions when the bubble's breakup can be observed are studied. Such description is obtained by analyzing the turbulent field around the bubbles. The structure of this thesis is the result of the need to simplify a complex system. The different mechanisms that appear in a stirred tank are analyzed separately in order to gain fundamental understanding of the different process involved. We simplify the geometry and considering a homogeneous isotropic turbulence instead the complex turbulent flow inside a stirred vessel. In such a way is the influence of the turbulent flow over the bubbles can be clearly observed.

Preface

Two-phase flows are abundant both in industry and nature. For this reason it is surprising that there still is a lack of knowledge and understanding about the basic mechanisms involved in the interactions among the dispersed and continuous phases, even nowadays. The capacity to estimate and describe the response of this kind of flows, both in theoretical and numerical models, would be of a great benefit in a variety of fields. For example in the atmosphere the turbulent flow can be "seeded" with small droplets which can fall down as heavy rain; in the dispersion of contaminants or in cooling columns in nuclear plants. All these type of flows share the same basic fundamentals: all of them consist of a turbulent continuous phase laden with suspended particles which can be distorted or not. The density of the particulate phase could be several orders of magnitude lower or higher that the carrier fluid. Further studies are needed to completely understand the physical mechanisms describing the interaction of turbulent flows and particles. The comprehension of the main mechanisms and their implementation can be useful in chemical engineering science, to scale-up process equipment or to improve mixing efficiency. Along this thesis diverse situations are studied, representing some of the most usual cases of the turbulent regime in two phase flows. We give some insight about the main physical mechanism involved, to contribute to the advance in the basic fluid mechanics field. This can be used as a basis to develop new theoretical models, validate data sets obtained via numerical simulations or to achieve closure conditions for the turbulent Navier-Stokes equations. The main motivation of this thesis is to provide a general view about different phenomenon in the interaction of particles and a turbulent flow. In all the cases studied here the particles are light and deformable namely bubbles, ranging from 2 to 4 mm in diameter. The bubbles move under the action of different turbulent conditions. In

most of the circumstances the turbulence is closely to isotropic. This is the 'simple' form of turbulence, if the expression is possible. One of the objectives of this work is to analyze a more complex turbulent flow; we consider stirred tanks in a two phase system. The experiments were conducted applying different measurement techniques widely used in fluid mechanics, as Particle Image Velocimetry (PIV) which allows to achieve a general picture of the flow field. This technique in combination with high speed cameras and Sensitive Hot Wire Anemometry permit us to obtain a robust set of measurements for all the conditions tested. Several analyzes are performed in the different chapters in which is specified when and why each of these techniques could be used.

The Thesis is organized as follows:

The first chapter is devoted to investigate the hydrodynamic characterization of stirred tanks under multiphase conditions (gas-liquid). The results are shown in terms of the power consumption performance of three axial impellers under different gas injection rates. All the cases are carried out in turbulent regime. The analysis includes the description of the flow patterns to recognize the conditions in which the bubbles' recirculations occur. In the second chapter of the Thesis we analyze the effect of bubble on a turbulent isotropic flow with mean average velocity. Results are obtained in an isotropic turbulent flow but the difference is that in such a case an augmentation in the amount of bubbles is presented allowing an increase in the gas void fraction and a parameter who characterize the quantity of agitation provided by the bubbles rising compared with the agitation provided by the turbulent flow is used, in the literature such parameter is called "bubblance". The aim of the chapter is to clarify the circumstances under the turbulence can be damped or enhanced. This can be identified in the slope change of the energy spectrum which characterizes the energy transfer of the system; many different couplings are presented between the two phases. In the third chapter experimental results are presented about the interaction of one single bubble with an isotropic turbulent flow. Two cases can be identified: in the first one the bubble breakup is observed and in the second one in which this does not occurs. The study proposes a quantitative description of the main mechanisms that start the breakage process and to identify the physical parameters that play a significant role in the deformation history. Finally in the last chapter a discussion and the main conclusions of the project are depicted, as well as some of the recommendations for future work.

Chapter **1**

Hydrodynamic Characterization of Three Axial Impellers under Gassed and Ungassed Conditions[†]

Abstract

We investigate the hydrodynamic performance of a baffled stirred tank for an air-water system in the turbulent regime. Comparisons among three different axial impellers were conducted: Maxblend impeller, two Pitched Blade Turbine (down-pumping mode) and two Intermig impellers. Measurements of the mean velocity field and the power consumption for gassed and ungassed conditions were obtained. The gas phase was introduced in a controlled manner using a capillary bank mounted at the bottom of the tank. The measured distributions of turbulent intensities for each impeller system for both gassed and ungassed configurations showed significantly different distributions. The flow patterns were drastically modified for gassed conditions for the conventional agitators. The Maxblend impeller was observed to maintain a certain degree of homogeneity in the turbulent distribution for both gassed and ungassed conditions.

1.1   Introduction

Fluid mixing is a fundamental operation in wide range of the industries [1, 2, 3, 6], usually performed by mechanical agitation. Stirred tanks are used for the homogenization of single or several phases. Typical examples are fermentation, crystallization, and polymerization, among others. A more advantageous option for specific operations can be achieved using different impeller geometries [6, 5]. Stirred reactors are often used for dispersing gases into liquids. Although traditionally many of these gas-liquid reactors are equipped with simple impellers like the radially pumping disc turbine, the development of pitched blade impellers has led to an increased interest in the use of axial flow impellers [6, 7, 8, 9]. The most common form of multiple impellers systems is the case of several agitators attached on the same shaft [10, 11, 12]. One of the most relevant parameters in a stirred tank is the power needed to produce fluid circulation into the vessel: the power draw is directly affected by the physical properties of the operating fluids, the impeller geometrical parameters and the flow regimes [8, 13, 14]. As a result, the power consumption affects the heat and mass transfer processes and, in a general manner, to the whole mixing process [12, 15, 16]. The influence of aeration on the power input to multiple impeller arrays have been studied in the past [5, 11, 12]. Various equations have been proposed to address the effect of the gas phase. The ratio Pg/Po, gas to ungassed power input, has been expressed as a function of dimensionless numbers to gain some understanding about the physical behavior of such systems [17, 18, 19]. Different states of gas dispersion within the vessel were first identified by Nienow et al. [3, 20] by visual observations, describing the states of gas dispersion within a gas-liquid stirred vessel provided of a single Rushton turbine. They identified five different regimes: 1) no gas dispersion, large bubbles are formed and rise along the impeller axis; 2) dispersion achieved only in the upper part of the vessel; 3) gas circulation observed in the upper part of the vessel with some circulation into the lower region; 4) circulation of bubbles throughout the vessel; 5) at higher impeller rotational speed, a secondary circulation loop of bubbles near to the surface. Three different hydrodynamic regimes were identified: flooding, loading, and complete dispersion, these regimes correspond to different types of interactions between the bubbles and the flow generated by the impeller [6].

Clearly the flow regime around the impeller influences the hydrodynamic within the vessel, the flow structure and the large-scale mixing performance into the tank. It has been found that the flooding phenomenon appears

when the power input by agitation is too low to disperse a certain gassing condition and the impeller is not able to handle the gas, which rises axially as a bubble column. Below this condition, gas dispersion becomes inefficient: the gas-liquid mass transfer rate decreases, and the sparged gas is not well distributed. Since the relation between power number and the Reynolds number is influenced by the hydrodynamic behavior, we can expect a strong influence of flooding on the patterns of a particular impeller.

In general, most studies have been conducted using small impellers (so called turbulent agitators); there is much less understanding of the performance of large impellers. Large agitators are usually provided with wide paddles [21, 22, 23] that promote strong flow circulations and dispersion of solid phase. Also some large impellers are equipped with grids that can induce folding of fluid elements. This type of impellers is well characterized and traditionally operated at the low range of Re numbers (laminar and transition regimes). The aim of this study is to investigate the performance of a wide impeller and compare it with conventional multiple impeller arrays for the case in which a gas phase is considered. We obtain a quantitative description of the single-phase flow and the gas-liquid flow of different axial impellers under various gassing conditions. Our attention is focused on the effect of gas phase on the change in the characteristics flow patterns, turbulence intensity distribution and power consumption.

1.2   Experimental Setup

Figure 1.1 shows the experimental setup, which consists basically of a tank and a velocimetry system. The particle image velocimetry (PIV) system was used to determine the flow field of the fluid phase alone [24]. *PIV* experiments were conducted at constant specific power draw (power per volume unit), for the different impellers under gassed and ungassed conditions. Fluorescent particles of 10 μm diameter *(Dantec Dynamics)* were used as tracer particles and the camera was equipped with a 680 nm optical filter, with the aim to separate tracer images from light scattered by the bubbles within the flow. The time between pulses was of the order of 1000 μs, using an adaptative correlation with interrogation areas of 32×32 square pixels and an overlap of $50 \times 50\%$ obtaining more than 3844 vectors for each acquired image. Acquisitions of 300 velocity fields were obtained using the phase-locking technique for each one of the cases analyzed in this study; in this

manner we obtained a statistically robust measurement of the mean flow. For this purpose an electronic shutter was placed in the impeller shaft and connected to the stirred system in such a way that the position of the impeller with respect to the camera and the baffles was always the same (90 degrees) at the measurements instant. Measurements were carried out in a tank with a semi-spherical bottom. The vessel was equipped with four planar baffles having a width of 13.2 mm. Fig. 1.2 shows the axial flow impellers used in this study: Maxblend impeller, two Pitched Blade Turbine in down-pumping mode and two Intermig impellers. The impeller shaft was driven by a variable speed motor, which was carefully controlled and measured. The stirred tank was filled with tap water. The geometrical parameters of the impellers and tank used in this work are presented in Table 1.1 for which D is the diameter, H is the height, C is the clearance and SR is the solidity ratio which is the ratio between the effective contacting area and the area of the projected circle in the axial direction defined as [6, 15]:

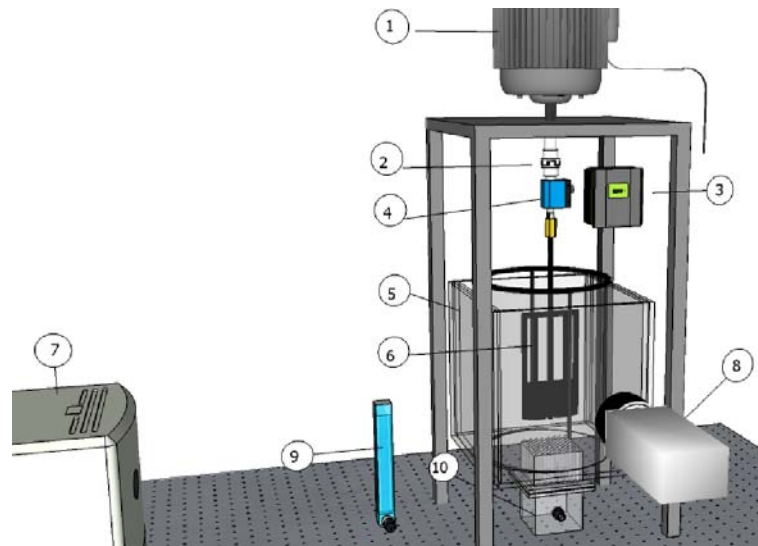$$SR = \frac{n_b A_b}{\frac{\pi}{4} D^2} \qquad (1.1)$$

Figure 1.1: Experimental setup. The camera was provided of a $680 n$m optical filter to acquire the velocity fluid phase and avoid liht scattered from the bubbles. 1) Motor, 2) flexible couple, 3) speed control, 4) torquimeter, 5) tank, 6) impeller, 7) laser, 8) camera, 9) gas flowmeter, 10) capillary bank.
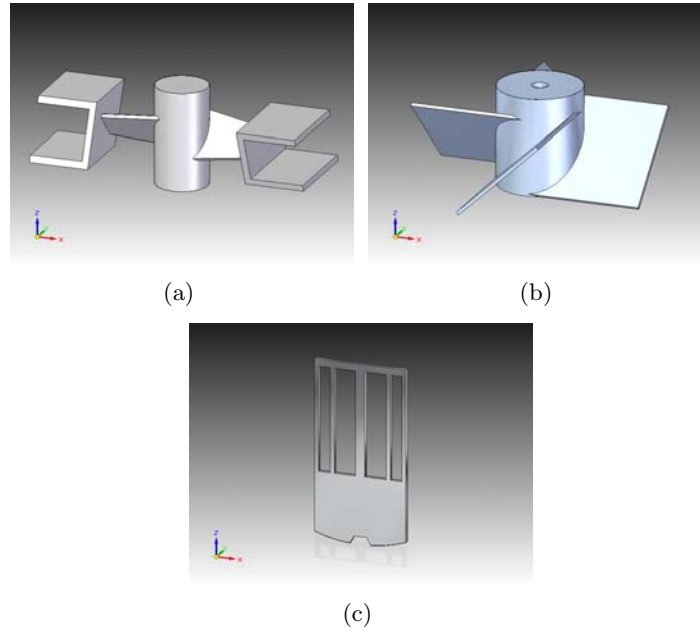
(a) (b)

(c)

Figure 1.2: Axial impellers used in this work, a) Intermig impeller, b) Pitched Blade Turbine, c) Maxblend impeller. The impellers dimensions are presented in Table 1.1.

(a) (b)
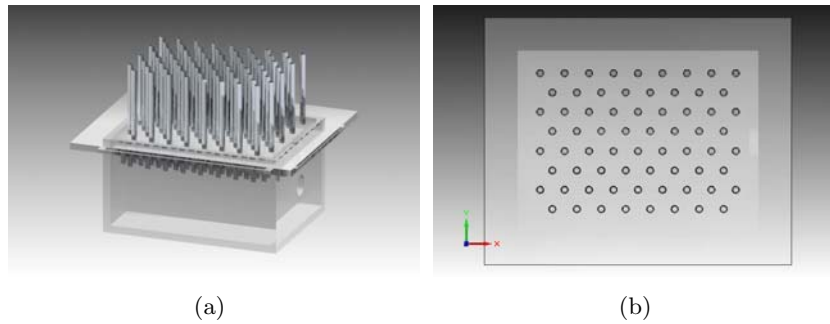
Figure 1.3: Capillary bank constituted by 56 capillary tubes, placed in a hexagonal array with an internal diameter of 0.36 mm. a)isometric view, b)top view.

where n_b is the number of blades and A_b is the area of the blades.

The experimental conditions are show in Table 1.2. For the two-phase experiments, gas was introduced at the center of the tank, below the impellers, through a capillary bank with 56 identical capillary tubes of 0.36

Agitator	$D(mm)$	$H(mm)$	$C(mm)$	$SR[-]$
Maxblend	88	162.7	5	3.76
2 PBTD	82.5	30	82.5	2.52
2 Intermig	82.5	18	82.5	1.3
Tank	165	198	-	-

Table 1.1: Geometrical Parameters of the impellers and the mixing tank.

Agitator	Parameter	PIV	Power Consumption
	Re	18,000	6,500 - 23,000
Maxblend	Gas Flow	0, 0.1, 0.3 vvm	0, 0.1, 0.3
	Spec. Power	0.1	0.005 - 0.2
	Re	32,000	3,000 - 35,000
2 PBTD	Gas Flow	0, 0.1, 0.3 vvm	0, 0.1, 0.3
	Spec. Power	0.1	0.003 - 0.44
	Re	35,000	12,000 - 50,000
2 Intermig	Gas Flow	0, 0.1, 0.3 vvm	0, 0.1, 0.3
	Spec. Power	0.1	0.005 - 0.34

Table 1.2: Conditions for PIV and Power consumption measurements.

mm in diameter placed in a hexagonal array (Fig. 1.3). The capillary bank produced bubbles with a diameter of about 2.5 mm. The flow rate was adjusted by a calibrated rotameter to impose two different gas flow rates injected into the vessel (0.1 vvm and 0.3 vvm).

Power draw measurements were performed for Reynolds numbers ranging from 3,000 to 50,000 for the three different impellers ungassed and gassed conditions. For that purpose, a torquemeter was placed between the motor and the impeller shaft.

The power consumption is characterized by the power number, N_p, which is defined as:

$$N_p = \frac{P_o}{\rho N^3 D^5} \tag{1.2}$$

where ρ is the fluid density; N is the impeller rotational speed and D is the impeller diameter. The character of the flow is determined by the Reynolds number, Re, defined as:

$$Re = \frac{\rho N D^2}{\mu} \tag{1.3}$$

where μ is the fluid viscosity. For the case of gassed systems we consider the gas flow number, defined as:

$$Fl_g = \frac{Q_g}{N D^3} \tag{1.4}$$

where Q_g is the gassing rate entering the vessel. This number compares the gas speed with respect to the characteristic speed of the fluid in the tank [25]. The turbulence intensity (TI), which can be derived from our experimental measurements, is defined as follows:

$$TI = \frac{\sqrt{v_x'^2 + v_y'^2}}{V_{tip}} \tag{1.5}$$

where $V_{tip} = ND$ is the impeller tip speed. TI can be interpreted as the amount of agitation produced throughout the stirred vessel, due to impeller action at certain mixing speed.

1.3   Results and Discussions

We present a description of the flow characteristics considering average velocity fields, turbulent intensities and power consumption. In all cases the single phase flows are used to compare the gassed configurations to assess the change of behavior resulting solely by the presence of the gas phase. It was found that the impeller type and both gassing rates can affect the overall behavior of the flow fields and the power consumption.

1.3.1   Flow Patterns and Mean Flow Fields

Figure 1.4 shows a comparison of the velocity magnitude fields generated by the three different impellers under ungassed and gassed conditions. As this figure shows, the horizontal and vertical dimensions are normalized using the radius of the tank; the color scale represents the velocity magnitude normalized by the tip velocity (V_{tip}). As we described before, the measurements for both conditions were obtained at 90 degrees, considering the same nominal power consumption (0.1 P/V).

The result for the Intermig impellers for ungassed conditions is illustrated in Fig. 1.4a. For the single phase condition this impeller creates a strong axial flow pattern and vortex regions are formed and are well defined. The main currents are located around the impeller and some weak flow regions (quasi-static and dead zones) are observed. In Fig. 1.4d we show the fluid behavior at high impeller speeds and low gassing rates ($0.1vvm$). In such a case the impeller pushes the fluid toward the vessel bottom. Also a strong radial flow generated by the mixed effects of fluid pushed down and away from the impeller is observed. In the upper side of the vessel, close to the upper impeller a strong axial flow is observed in the upward direction near to the vessel wall, which is mainly due to the fluid drag by the bubbles rising through the vessel and a radial discharge of the impeller. A small vortex zone is observed in the upper part of the vessel. Fig. 1.4g at the highest gas flow rate (0.3 vvm). The flow pattern is similar to the previous case but some slight differences can be appreciated. A decrease in the radial flow and in the amount of fluid pushed away by the impeller to the bottom of the tank is observed. Also the small vortex zone in the upper part of the vessel is reduced and an increase in the upwards vertical current is also observed. The change in the flow pattern can be explained due to the increasing gas flow rate and the decreased gas handling capacity of this impeller. As the gassing rate is increased the impeller is not capable to disperse the gas phase. At medium and high gassing rates the impeller is not able to deflect the rising gas flow and gas raises upwards directly. In this situation the flow pattern is dominated by the rising gas flow rather than by the impeller. This situation is often called flooding.

Figure. 1.4(a,d,g) also show the measured average velocity field for the Intermig impeller, for the ungassed and gassed configurations. The distribution of velocity magnitudes for the ungassed case is modified considerably. Clearly, we can identify two high velocity regions, one in the middle of the
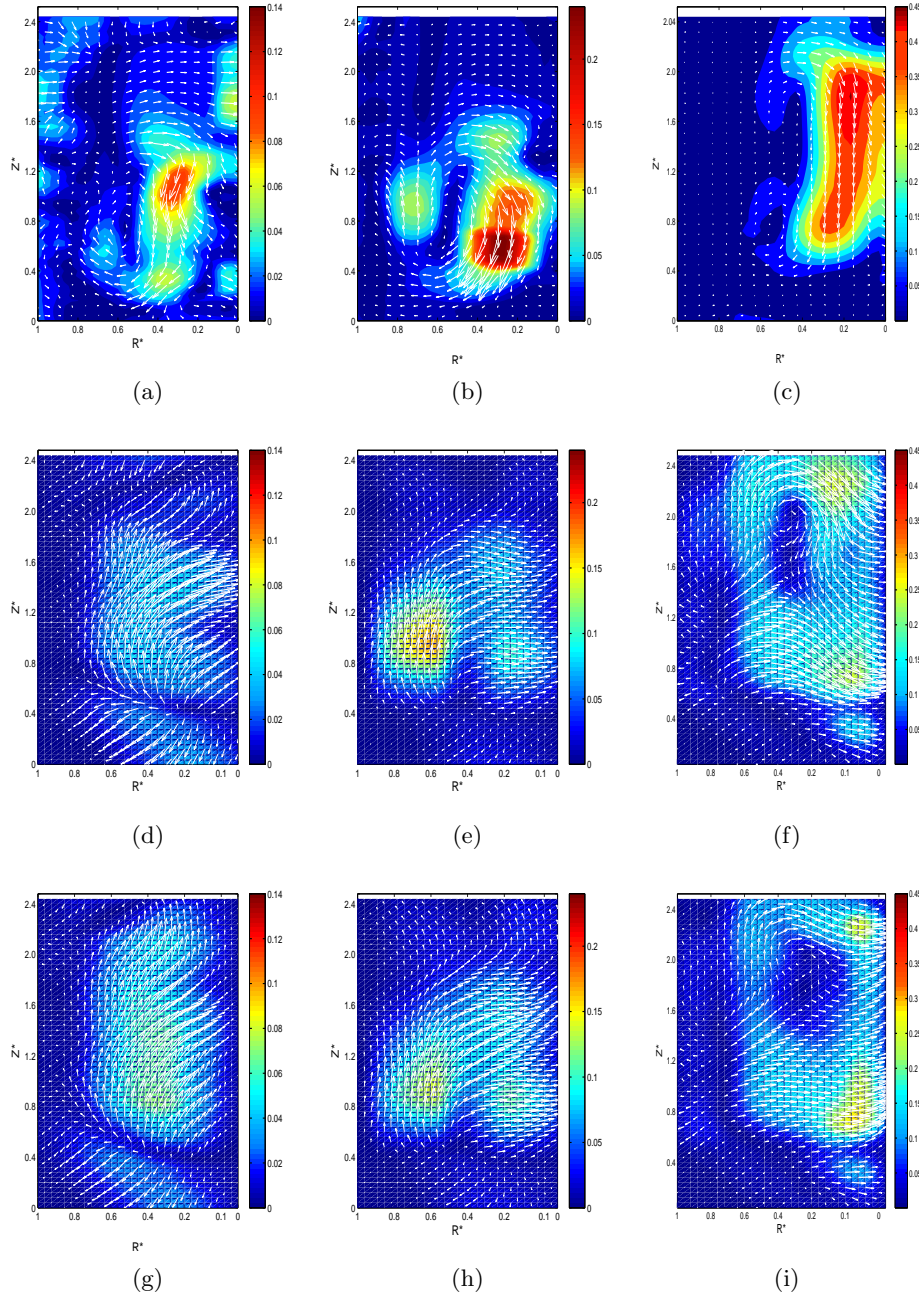
Figure 1.4: Magnitude velocity fields for the three different impellers in the flow regimes investigated. The color scale shows the velocity magnitude normalized by V_{tip}. Note that each impeller (each column) has its own scale: Intermig, (a) single phase, (d) 0.1 vvm, (g) 0.3 vvm; PBT, (b) single phase, (e) 0.1 vvm, (h) 0.3 vvm; Maxblend, (c) single phase, (f) 0.1 vvm, (i) 0.3 vvm.

tank and the other one near the bottom. These zones correspond to the impeller positions mounted in the same shaft, as the flow in the center region of the container is basically axial-upwards. We can infer that this high flow zone is generated mainly by the bubbles moving to the free surface. The impeller, in the bottom of the container, is not able to dispersed the gas. We can observe a high velocity gradient region in the bottom part of the tank. This flow corresponds to the fluid and the bubbles displaced by the agitator mounted near the gas injection region. As the gas flow rate is increased (0.3 vvm), the zone of large velocity magnitude in the bottom part of the vessel decreases at least at 20%, although in the central part the flow increase near to a 50%. We can conclude that such flow is generated due to the increase of the gas flow rate and the impellers are not suitable to handle this amount of gas and most of the bubbles flood the upper impeller. In this case, the bubbles rise freely without any interaction with the agitators.

Figure 1.4(b,e,h) shows the results for the PBT impeller. The flow patterns in the single-phase for the Intermig and the PBTD impellers are similar but the velocities are slightly smaller in the latter (Fig. 1.4). Note also that the center of the large circulation loops for the PBTD case is shifted slightly upwards. The main difference is that with PBTD no circulation below the impeller was observed. With the PBTD, there is also a second recirculation loop in the upper part of the vessel. Interestingly the flow pattern measured for the PBTD turned out to be very sensitive to the injected gas flow rate as show in Figs. 1.4e and 1.4h. As a result of the injected gas, the flow pattern is modified drastically. Once the gas is injected the flow pattern does not change even by increasing the gassing rate. The main difference is the presence of a small secondary loop near to the upper impeller in the Intermig configuration. In the same manner that for the case of the PBTD, we can observe how the impeller pushes the fluid to the bottom of the vessel, but the radial flow in the direction of the impellers rotation is also important. On the other hand, in the region away from the impeller zone, the bubbles rise to the free surface, showing the ineffectiveness of the impeller under gassed conditions. Such a behavior is observed with the Interming and PBTD configurations. With these conventional impellers under gassing conditions the main axial flow pattern change drastically.

The effect of the aeration upon the mean velocity field for the PBTD impellers are show in Fig. 1.4(b, e, h), corresponding to the gassing rates 0, 0.1 and 0.3 vvm respectively. At low gas flow rate, the velocity distributions change substantially from the ungassed condition, a large recirculation loop

appears. The highest velocity under the up-pumping mode is found near the vessel wall. We can observe that the amount of fluid pumped by the lower impeller is less compared to the Intermig case, in which the fluid and the bubbles are pushed toward the vessel bottom. The bubbles rise along the vessel wall and just a little amount of gas is driven by the upper impeller. As the gas flow rate is increased the velocity flow field is similar to the previous case without any noticeable change or increase in the magnitude velocities. Upon gassing, a large upwards flow is generated in the region bellow the impeller due to the action of the bubbles. These effects result in an enhanced axial upwards flow near to the impellers in the central region.

Figure 1.4(c, f and i) show the velocity field obtained with the Maxblend impeller under ungassed and gassed conditions, respectively. We can observe vertical currents generated from the top to bottom, induced by the impeller's paddle; the flow moves upward near the vessel wall and downward in the center of the vessel. A small vortex ring is observed above the agitator and the fluid flows axially along the impeller shaft, which is in agreement with previous experimental findings reported elsewhere [26]. Also a second recirculation loop forms in the upper part of the vessel, and the flow along the wall in the top of the vessel is redirected upwards. As Figs. 1.4f and 1.4i show, a vortex in the upper part of the vessel (in the grid part of the impeller); a main axial flow is generated in the center of the tank along the impeller shaft. Part of the fluid is pumped in the radial direction by the paddle part of the impeller. As the gas flow rate is added, the vortex in the upper part of the vessel is partly dissipated and its intensity decreases. The axial flow in the impeller shaft almost vanishes and the radial flow increases. As the gassing rates increases the flow pattern switches from axial flow to radial flow. Therefore, this impeller is still able to handle this amount of gas, increasing the resident time of the gas into the container. For such high gas flow rates, the recirculation zones reduce in size and the principal axial flow is gradually modified. Such a behavior was observed for both gas flow rates of 0.1 and 0.3 *vvm*.

For gassed conditions the Maxblend impeller shows the higher values of magnitude velocities and a more homogeneous distribution compared to the other impellers (Intermig and PBT), confirming that the geometry plays an important role in fluid flow along the tank. For this condition the velocity magnitude distributions were altered at low gas fraction (0.1 *vvm*), two important high velocity regions are presented. These zones are connected into a loop forming a large vortex that occupies the most part of the container.

For the highest gas flow rate condition (0.3 vvm), the dominant loop is also present but the intensity of the velocity decreases. The major part of the fluid is still influenced by the impeller and just a little gas volume will rise upward without restraint in the wall of the container. The flow recirculation induced by the agitators is evident. For the Maxblend case (Fig. 1.4(c, f, i)), we can identify large vortex structures at the top and bottom of the impeller. These vortical structures induce vertical currents that cause mixing between the different layers of the fluid promoting gas dispersion. For the cases of the two Intermig impellers and two PBTD (Fig 1.4(d,g) and 1.4(e,h)) the main velocity regions are located in the near to the upper impeller due to the rising bubbles and near the walls. The velocity induced in the fluid phase is larger for the case of the Maxblend impeller for both levels of the gas flow rates. For the three impellers, the normalized liquid velocities (V/V_{tip}) are larger than the ones obtained under ungassed conditions. From these results, it is interesting to note that the characteristic flow patterns of the PBTD and the Intermig impellers under the same gas conditions are very similar, but that the flow pattern found with the Maxblend impeller is quite different. Comparing the gassed cases with the single phase case, the change in the Maxblend impeller is smaller compared to the other impellers. Clearly the geometry of the Maxblend impeller influences strongly the mixing performance and the flow patterns generated in the turbulent regime under gassed conditions.

1.3.2   Turbulent Intensities

Similar to single-phase mixing processes, in liquid-gas mixing applications the degree of agitation, characterized by the turbulent intensity [27, 26, 28], is of great importance. In such systems a high turbulent intensity will lead to increased bubble break up, which may affect the mixing of the process. The turbulent nature of the flow has been characterized by the spatial distribution of local turbulent intensity. Large velocity gradients produce large velocity fluctuations, which lead to an increase of turbulence intensity. Fig. 1.5 shows the turbulence intensity distribution maps, for the Intermig and the PBTD impellers. A region of high values of turbulence intensity is found above and below the impellers. This is probably due to the large velocity gradients near to the center of the circulation vortex below the impeller. For both impellers the turbulence distribution is far from homogeneous. For both cases the highest turbulence intensities are found in the outflow region of the impellers; turbulence intensity is much lower in the bulk of
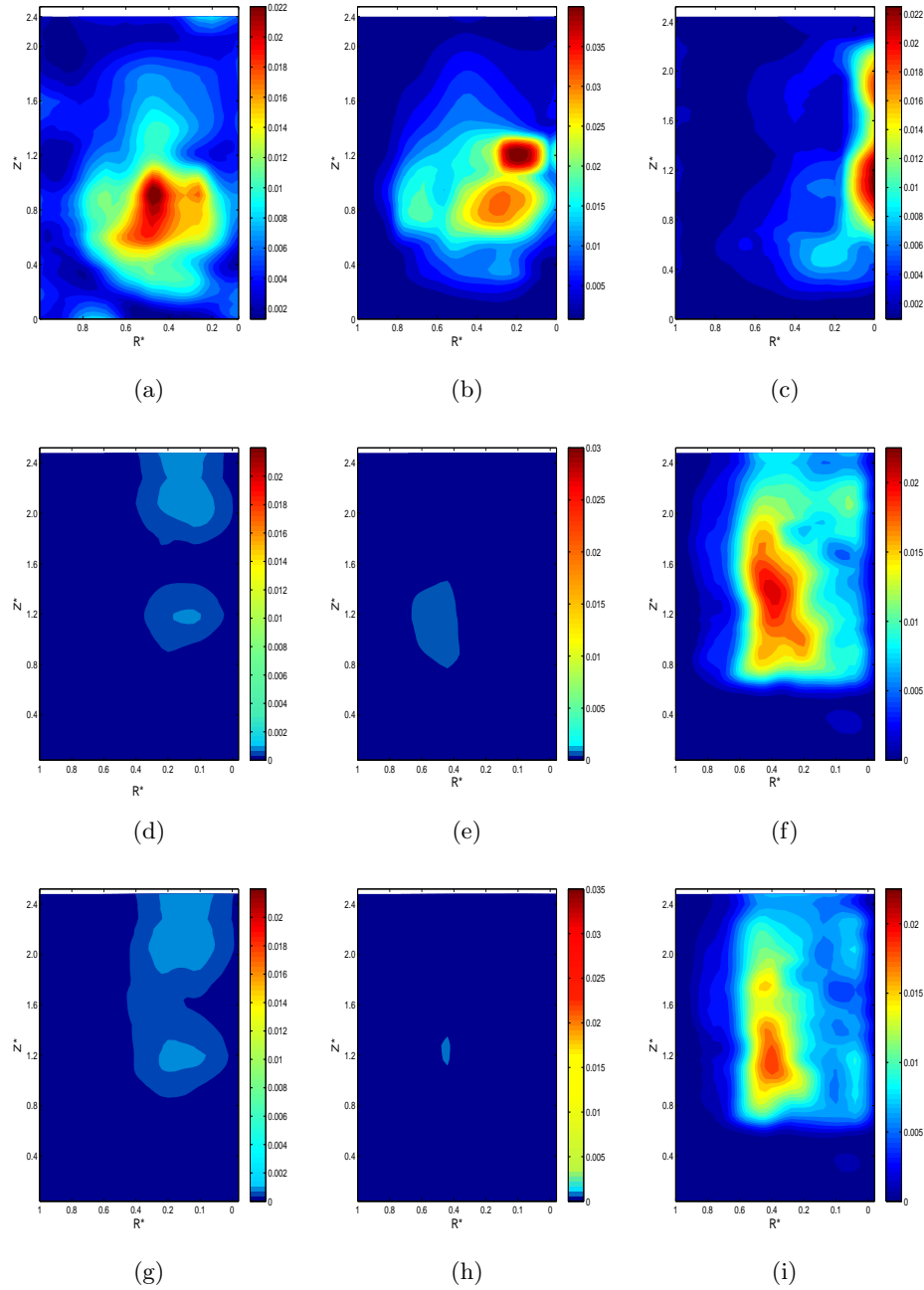
Figure 1.5: Turbulent intensity for the three impellers in the flow regimes investigated. The color scale shows the turbulent intensity. Note that each impeller (each column) has its own scale: Intermig, (a) single phase, (d) 0.1 vvm, (g) 0.3 vvm; PBT, (b) single phase, (e) 0.1 vvm, (h) 0.3 vvm; Maxblend, (c) single phase, (f) 0.1 vvm, (i) 0.3 vvm.

the tank. In the Maxblend case we can observe an important difference. As Fig. 1.5(f,i) shows the distribution of the turbulent field is nearly homogeneous and covers a large part of the tank, and the intensity is higher than that found for the other impellers tested. The turbulent intensity distributions for the gassed condition are show in Fig. 1.5(f,i). At low gassing rate (0.1 vvm), the turbulent distribution for the Intermig impeller is also non-homogeneous. Significant differences in bubble breakup throughout the vessel are observed. The gas accumulates in the outflow regions of both impellers, where turbulence levels are large. This leads to an increase in bubble dispersion. As the gas rate is increased (up to 0.3 vvm) the turbulence distribution remains nearly unchanged. Fig. 1.5(b,e,h) shows the turbulent intensity fields for the PBTD impeller, where the flow structure generated at 0.1 vvm leads to a clearly defined distribution of the turbulent intensities larger compared to the single-phase system. It can be seen from Fig. 1.5(b,e,h) that high turbulent intensity is observed in the outflow of the lower impeller. As the gas flow rate is increased, the region of turbulent intensity increases in size and a significant amount of turbulence generation in the upper part of the vessel is generated. As a result of the gas injection, the turbulence distributions for the pitched blade turbine in the down pumping mode and the Intermig impellers are quite different from the ungassed system for both impellers described before. For this type of impellers the turbulence levels in the impeller zones are always be stronger than in the liquid bulk due to blade actions and shear rates generated.

The Maxblend turbulent distribution under gassed conditions at 0.1 vvm is still characterized by a high degree of homogeneity throughout the entire vessel. High levels of turbulent intensity are observed around the grid part of the impeller in the middle of the vessel. At 0.3 vvm gas flow rate the turbulent distribution maintains its structure and is concentrated in the impeller area, but a slight decrease in the intensity is observed. On the other hand the Intermig impellers do not yield to large values of turbulent intensity, and the PBTD impeller reduces its capacity to homogenize the flow, while the Maxblend produces large velocity fluctuations for both low and moderate gas flow rates.

1.3.3   Power consumption and flow number

In mixing processes the energy requirements needed to achieve a good dispersion and homogeneous mixing plays an important role when scaling up

mixing systems. In such cases the power consumption is determined by the energy transferred by the impeller to the fluid. As expected, when the power draw by the impeller increases as its rotational speed increases. In this manner the power input is a function of the impeller geometry, the baffle configuration, and obviously the physical properties of the fluid. In mixing operations, the flow regime is characterized by the Reynolds number, Re. The power consumption (P_o) is usually expressed in its dimensionless form by the power number, N_p, (Eqn. (1.2)). Fig. 1.6 shows the power number of the three axial impellers, under gassed and ungassed conditions. This plot depicts the energy transferred from the impeller to the fluid, which approximately remains constant in the turbulent regime. The performance of different agitators is strongly dependent on their geometries. Under gassed conditions, no significant differences were found for the Intermig impellers. For the Maxblend impeller, a slight decrease of the order of 8 % and 18 % at 0.1 and 0.3 *vvm* respectively, was noticed; for the Intermig impeller under the gassing action, power consumptions is the same (within the measurement uncertainty) for both gassing rates 0.1 and 0.3 *vvm*, compared with the ungassed regime. The PBTD impeller exhibits a similar behavior; in this case the power draw reduction was calculated at 9 % and 13 % at 0.1 and 0.3 *vvm* gas flows. However, the slight differences between the performance of the impellers at ungassed and gassed conditions under the various flow gas regimes do not necessary suggest that the agitators can handle large amounts of gas. Bakker et. al 1994, concluded that an agitator with a large solidity ratio is capable to work at high gas loading. It can be seen in Table 1.1 that the Maxblend impeller, compared with the Intermig impeller and the PBTD, has the largest solidity ratio but the difference in blade area between conventional impellers is also notable. To fully analyze the performance is necessary to consider also the flow patterns (and possibly the pumping capacity). When the impellers are not able to handle the gas phase at a constant gassing rate, the bubbles flowing from the vessel bottom pass throughout the agitators without any interaction with the fluid pushed away by the impeller. In that case, the gas dispersion is undesirable and the power remains unchanged and a large difference is not observed; therefore, the impeller is flooded. For gas-liquid systems is necessary to take into account the effect of the dispersed gas in the agitator performance since the point of view of the power draw. In this sense is useful to quantify the amount and circulation of gas phase. The flow number (Fl_g) is important to characterize the flow phenomena occurring in the impeller region. It accounts for the effect of gassing rate, impeller speed and impeller diameter.
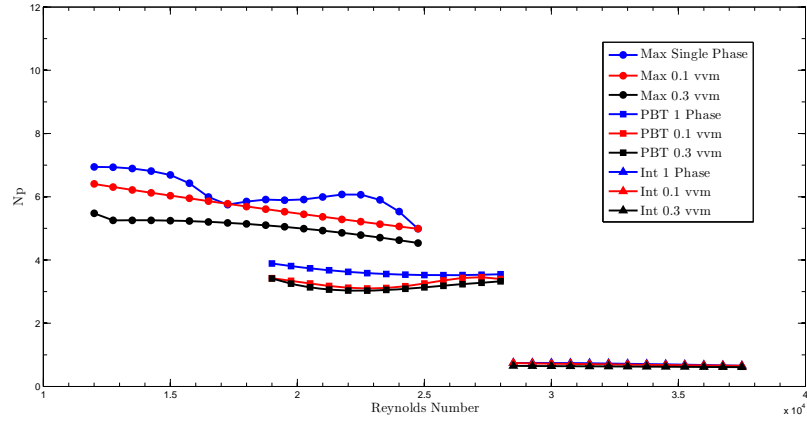
Figure 1.6: Power Number of the three axial impellers, under gassed and ungassed conditions.

### 1.3.4   Effect of the gassing on the Power Consumption

The response of power consumption on gassing rates is closely related to the modifications on the hydrodynamics around the impeller and the flow patterns previously discussed. Such performance can be quantified by analyzing the ratio of gassed to ungassed power consumption (P_g/P_o) as a function of the Gas Flow number (Fl_g) defined before Eqn. (1.4). Fig. 1.7(a,b and c) show this ratio for each one of the impellers used. Fig. 1.7a shows the results for the Intermig impeller quantitatively for the two distinct gas flow rates ($0.1vvm$ and $0.3vvm$). When a low gas flow rate is injected ($0.1vvm$) and the impeller speed increases the (Fl_g) number (increase of the impeller speed) the gassed to ungassed ratio decreases until a minimum and grows again. This could be attributed of a decrease of the cavity sizes and the gassed power consumption augment showing that when the speed is fast enough this kind of impeller is able to handle this low amount of gas. When the gas flow rate is increased to $0.3vvm$ the response is similar; it is necessary to achieve a higher impeller speed. For the latter case a diminishing of the power ratio is still present, this could mean that gas recirculation is not achieved. Fig. 1.7b illustrates the relation between the ratio P_g/P_o at two constant gas flow rates ($0.1vvm$ and $0.3vvm$) for the PBT impeller. For this impeller at the low gas flow rate ($0.1vvm$) the power consumption shows a steep decrease, related with the direct-indirect loading transition, which

depends on the impeller speed. For the higher gas flow rate the behavior is similar to that for the greater gas value for the Intermig impeller, showing that for this flow regime both impellers are not capable to manage this gas rate, and the complete recirculation is not reached. The trends in the gassing to ungassing ratios in the higher gas rate for the PBT impeller and the Intermig impeller are similar, although more pronounced in the latter one. Fig. 1.7c shows the P_g/P_o ratio at two different constant gas flow rates corresponding to $0.1vvm$ and $0.3vvm$ at different impeller speeds for the Maxblend impeller. The different regions in this curves corresponds to the three different flow patterns of the three states of dispersion discussed before. As in the case of the PBT impeller at $0.1vvm$ the large cavities are formed corresponds to a large drop in the power consumption. From the results depicted in Fig. 1.7c an increase in the power ratio with a reduced gas flow rate is observed. Another trend is appreciated for the Maxblend impeller at both gassing rates. For the two gassing rates the behavior is quite similar and no substantial change in the trends are noted. Furthermore, comparing gassed to ungassed ratio, in the final part of the curves at low gassing rates (at high rotational speed) an augmentation in values are caused by the cavity formation behind the bottom part (paddle part) of the impeller are presented. We can assume for the impellers described before that no complete dispersion is achieved, what is opposed for the Maxblend case, the curves show only depends on the impeller speed and the flooding-loading conditions can be identified clearly from the slope change of the curves in each case.

For the conditions tested here the transition between the different gas dispersion states occur at the higher flow numbers (in comparison with the turbulent impeller). This means that lower impeller speeds are needed [7]. In a general manner we can concluded that the ratio of gassed to ungassed power is a good parameter to determine the performance of different impellers in a comparative way. The perform will depend on the impeller type, gas flow rates and the injection gas device. The whole configuration determines the different transition zones in dispersed systems, due to various induced flow patterns and cavity shapes created.
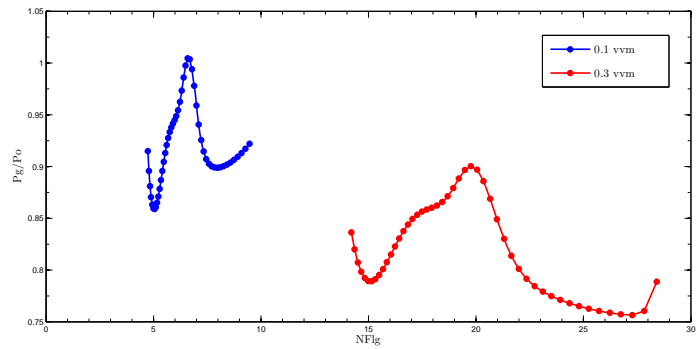
1.4 Conclusions

The objective of this investigation was to experimentally determine the flow and mixing performance of three different axial impellers under gassed and ungassed conditions in the turbulent regime. The results obtained in two
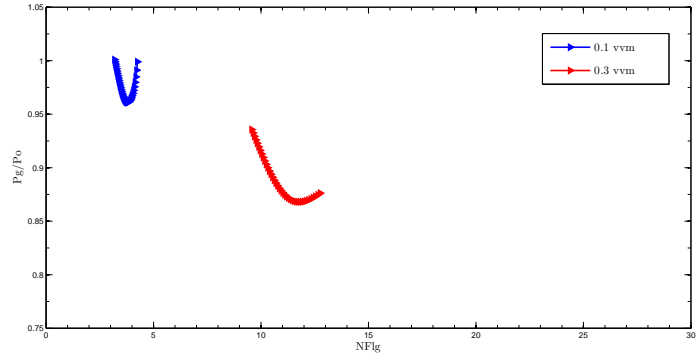
(a)
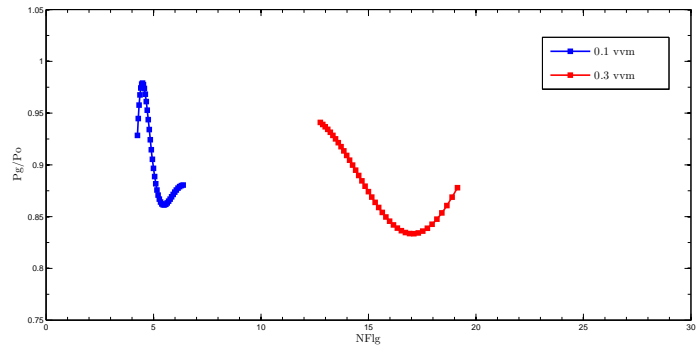
(b)

(c)

Figure 1.7: Ratio of Gassed to Ungassed Power Consumption as a function of Gas Flow Number for the different impellers, a) Intermig impeller, b) PBT impeller, c) Maxblend Impeller.

phase cases showed a slight reduction in power consumption in comparison with single phase case. The drop in power consumption upon gassing conditions was found to be modest, with no appreciable decrease in the turbulent regime. These results are unexpected as larger power draw could be expected. The different performance can be explained in terms of the different gas injection device used in this work. Our findings confirm the current discussion in the literature: the power consumption is very sensitive to the configuration of the gas injection.

Using a *PIV* system, the flow patterns induced by the three agitators were studied. The single-phase flow is characterized by the formation of several recirculation zones around the impeller. These flow patterns were reported in the past. To our knowledge the effect of having a second gas phase had not been addressed in detail before. We found that the gas can drastically change the flow patterns, particularly for conventional impellers (Intermig and PBTD). This pattern deviation suggests that these agitators are not able to handle the gas flow rates considered here; the Maxblend impeller also changes its single-phase flow behavior under gassing conditions but in a modest manner. The main axial flow is deviated and it becomes mainly radial at the highest gas flow rates, but some high vorticity zones and large axial currents are still present. From these results we can infer that for the two gassing flow rates the Maxblend impeller is capable to manage the gas, having an acceptable performance.

The turbulence distribution of the Intermig and the PBTD impellers are far from homogeneous. Also, the magnitude of turbulent fluctuation is moderate for the single phase flow. Under gassing condition the level of turbulence is further reduced. The Maxblend impeller single-phase performance in turbulent condition creates large and homogeneous regions. When the gas phase is added these turbulent regions remain in large parts of the vessel.

In general we can conclude that the gassed power consumption depends on the type of the impeller and the overall system configuration, due to the different type of the structures created. The impellers are also compared in terms of the power consumption necessary to achieve a complete dispersion. Comparing the three impellers analyzed under the gas flow conditions studied here, the Maxblend impeller shows an easy transition to the axial to the radial flow pattern. A slight difference between the PBT and the Intermig impellers is observed, but at high gas flow rates the Maxblend impeller exhibits a better performance. In other words, this impeller is capable to maintain a stronger liquid flow than the other agitators.

Nomenclature

- A_b area of the blades (mm^2)

- C impeller clearance (mm)

- D impeller diameter (mm)

- Fl_g gas flow number (-)

- H impeller/vessel height (mm)

- N impeller rotational speed (s^{-1})

- n_b number of blades (-)

- N_p dimensionless power number (-)

- P_g gassed impeller power consumption (W)

- P_o ungassed impeller power consumption (W)

- Q_g gas flow rate (vvm) (volumetric gas flow rate/min)/volume of liquid

- Re impeller Reynolds numer (-)

- SR solidity ratio (-)

- TI turbulent intensity (-)

- V_{tip} impeller tip velocity ($m\ s^{-1}$)

- $v^{'}$ velocity fluctuation ($m\ s^{-1}$)

Greek Symbols

- μ fluid viscosity, $kg\ m^{-1}s^{-1}$

- ρ fluid density, $kg\ m^{-3}$

Bibliography

[1] Joshi, J. B.; Pandit, A. B.; Sharma, M. M. Mechanically agitated gas-liquid reactors. Chem. Eng. Sci. 1982, 37:813-844.

[2] Mann, R.; and Hakett, L. A. Fundamentals of gas-liquid mixing in a stirred vessel: An analysis using networks of zones. Proceeding 6th Eur. Conf Mixing; Pavia, Italy. 1988, 24-26, 321-328.

[3] Nienow, A. W., Harnby, N.; Edwards, M. F. Mixing in the Process Industries, Second Edition, Butterworth-Heinemann. 1997.

[4] Tatterson, G. B. Fluid Mixing and Gas Dispersion in Agitated Tanks, Mc Graw-Hill, Inc. 1991.

[5] Zlokurnik M., Stirring, Theory and Practice, Wiley-VCH Verlag GmbH, 2001.

[6] Bakker, A.; Van den Akker, H. E. A. The use of profiled axial flow impellers in gas-liquid reactors. Proc. Fluid Mixing IV, Bradford, UK .IChemE Symposium Series 121, 1990, 153-166.

[7] Bakker, A.; Van den Akker H.E.A. Gas-Liquid Contacting with Axial Flow Impellers. Chemical Engineering Research and Design, TransIChemE, Number A4, 1994, 72, 573-582.

[8] Kresta, S.; Wood, P. E. The mean flow pattern produced by a 45 pitched blade turbine: change in the circulation pattern due to off bottom clearance. Can. J. Chem. Eng. 1993, 71, 42-53.

[9] Warmoeskerken, M. C. G.; Speur, J.; and Smith, J. M. Gas-liquid dispersion with pitched-blade turbines Chem. Eng. Comm., 1984, 25: 11-29, 350.

[10] Markopoulos, J.; Pantuflas, E. Power consumption in gas-liquid contactors agitated by double-stage Rushton turbines. Chem. Eng. Tech. 2001. 24, 17, 1147-1150.

[11] Rutherford, K.; Mahmoudi, S. M. S.; Lee, K. C.; Yianneskis, M. Hydrodynamic characteristics of dual Rushton impeller stirred vessels. Am. Ins. Chem. Eng. J. 1996, 42, 332-346.

[12] Taghavi, M.; Zadghaffari, R.; Moghaddas, J.; Moghaddas, Y. Experimental and CFD investigation of power consumption in a dual Rushton turbine stirred tank. Chem. Eng. Res. and Des. 2011, 89, 280-290.

[13] Devals, C.; Heniche, K.; Takenaka, K; and Tanguy, P.A. CFD analysis of several design parameters affecting the performance of the Maxblend impeller. Comp. and Chem. Eng. 2007, 32, 1831-1841.

[14] Fradette, L.; Thom, G.; Tanguy, P.A.; and Takenaka, K. Power and Mixing time study involving a Maxblend impeller with viscous Newtonian and non-Newtonian fluids. IChemE, 2007, 85(A11), 1514-1523.

[15] Oldshue, J. Y.; Post, T. A.; Weetman, R. J.; and Coyle, C. K. Comparison of mass transfer characteristics of radial and axial flow impellers Proceedings 6th Eur. Conf Mixing, Pavia, Italy, May. 1988, 22-24, 345.

[16] Sommerfeld, M.; Decker, S. State of the art and future trends in CFD simulation of stirred vessel hydrodynamics. Chem. Eng. and Tech. 2004, 27, 215-224.

[17] Chapman, C. M.; Nienow, A. W.; Cooke, M.; and Middleton, J. C. Particle-gas-liquid mixing in stirred vessels; Part 2: Gas-liquid mixing. Chem. Eng. Res. Des., 1983a, 61: 82-95.

[18] Chapman, C. M.; Nienow, A. W.; Cooke, M.; and Middleton, J. C., Particle-gas-liquid mixing in stirred vessels; Part 4: Mass Transfer and Final Conclusions. Chem Chem. Eng. Res. Des., 1983b, 61: 182-185.

[19] Laufhütte, H. D.; and Mersmann, A. B. Dissipation of power in stirred vessels Proceedings 5th Eur. Conf Mixing, Wurzburg, Germany. 1985, 10-12, 331-340.

[20] Nienow, A. W.; Konno, M; and Bujalski, W. Studies on three-phase mixing: A review and recent results. Chem. Eng. Res. Des. 1986, 64:35-42.

[21] Bertrand, F.; Tanguy, P. A.; Brito de la Fuente, E.; and Carreau, P. Numerical modeling of the mixing flow of second-order fluids with helical ribbon impellers. Computer Methods in Applied Mechanics and Engineering, 1999, 180, 267-280.

[22] Iranshahi, A.; Devals, C.; Heniche, M.; Fradette, L.; Tanguy, P. A.; Takenaka, K. Hydrodynamic characterization of the Maxblend impeller. Chem Eng Sci. 2007, 62, 3641-3653.

[23] Rivera, C. A.; Heniche, M.; Takenaka, K.; Tanguy P. A. Finite element modeling of the laminar and transition flow of the Superblend dual shaft coaxial mixer on parallel computers. Chem Eng. Science. 2009, 64, 4442-4456.

[24] Myers, K. J.; Ward, R. W.; Bakker A. A digital particle image velocimetry investigation of flow fields instabilities of axial-flow impellers. ASME J. Fluids Eng. 1997,119, 623-632.

[25] Smith, J. M. Dispersion of gases in liquid Mixing of Liquids by Mechanical Agitation, Eds. Ulbrecht J. J. and Patterson G. K., Gordon and Breach Science Publishers. 1985.

[26] Hidalgo-Millán, A.; Zenit, R.; Palacios, C.; Yatomi, R.; Horiguchi, H.; and Tanguy, P.A; Ascanio, G. On the hydrodynamics characterization of the straight Maxblend impeller with Newtonian fluids. Chem. Eng. Res. and Des. 2012, 90, 9, 1117-1128.

[27] Camacho-Martínez, J.L.; Ramírez-Argaez, M.A.; Zenit-Camacho, R.; Juárez-Hernández A.; Barcenas-Sánchez, O.; Trápaga-Martínez, G.; Physical Modelling of an Aluminum Degassing Operation with Rotating Impellers a Comparative Hydrodynamic Analysis Materials and Manufacturing Processes. 2010, 25, 581-591.

[28] Kresta, S. Turbulence in stirred tanks: anisotropic, approximate and applied. Can. J. Chem. Eng. 1998, 76, 563-576.

Chapter 2

Energy Spectra in Bubbly Turbulence[†][‡]

Abstract

We conduct experiments in a turbulent bubbly ow to study the unknown nature
of the transition between the classical $-5/3$ energy spectrum scaling for a single-
phase turbulent flow and the -3 scaling for a swarm of bubbles rising in a quiescent
liquid and of bubble-dominated turbulence. The bubblance parameter ([5, 16]),
which measures the ratio of the bubble-induced kinetic energy to the kinetic en-
ergy induced by the turbulent liquid fluctuations before bubble injection, is used
to characterise the bubbly flow. We vary the bubblance parameter from $b = \infty$
(pseudo-turbulence) to $b = 0$ (single-phase flow) over 2-3 orders of magnitude: $\approx O$
(0.01, 0.1; 5) to study its effect on the turbulent energy spectrum and liquid veloc-
ity fluctuations. The experiments are conducted in a multi-phase turbulent water
tunnel with air bubbles of diameters 2-4 mm and 3-5 mm. An active-grid is used
to generate nearly homogeneous and isotropic turbulence in the liquid flow. The
liquid speeds and gas void fractions (α) are varied to achieve the above mentioned
b parameter regimes. The experiments employ a phase-sensitive Constant Tem-
perature Anemometry (CTA) technique, which provides $in-situ$ flow information
to help discard bubble collisions. The probability density functions (PDFs) of the
liquid velocity fluctuations show deviations from the Gaussian profile for $b > 0$, i.e.
when bubbles are present in the system. The PDFs are asymmetric with higher
probability in the positive tails. The net liquid fluctuations in the system slightly

increase with the b parameter (when $b < 1$) and then saturate for $b > 1$. The energy spectra are found to follow the -3 subrange scaling not only in the well-established case of pseudo-turbulence, but in all cases where bubbles are present in the system ($b > 0$), in the present parameter regime. It is remarkable that this -3 scaling is followed even for small b parameter values (b $\sim O(0.01)$). This implies that the bubbles are extremely efficient in leaving their spectral signature in the flow, presumably due to the long lifetime of the bubbles' wake. The -3 spectrum scaling thus seems to be a generic feature of turbulent bubbly flows.

2.1   Introduction

Turbulent bubbly flow has important industrial applications such as in chemical industries and steel plants ([3]). A fundamental understanding of the influence of bubbles on turbulence is crucial for better designs and optimal utilization of resources ([6, 4]). The fundamental question we study in this work is: How do bubbles modify the turbulence? - i.e. what is their effect on the turbulent energy spectrum and liquid velocity fluctuations. The source of energy input in turbulent bubbly flows can have a contribution from both bubbles and some other external forcing (which affect the liquid fluctuations). Depending on this source of energy input, we can have various regimes in turbulent bubbly flows. The bubblance parameter "b" was introduced ([5, 16]) to distinguish between the regimes of pseudo-turbulence (i.e. turbulence driven solely by bubbles rising in a quiescent fluid) and turbulence induced by liquid fluctuations alone. The bubblance parameter is defined as a ratio of the bubble-induced kinetic energy to the kinetic energy induced by the turbulent liquid alone without bubbles:

$$b = \frac{1}{2}\frac{\alpha U_r^2}{u_0'^2} \tag{2.1}$$

where, α is the bubble concentration (void fraction), U_r is the bubble rise velocity in still water, and $u_0'^2$ is the typical turbulent liquid fluctuation in the absence of bubbles. The extreme cases are $b = 0$ for single-phase turbulent flow (i.e. bubbles being absent in the flow) and $b = \infty$ for pseudo-turbulence.

Pioneering measurements by [5] used hot-wire and Laser Doppler Anemometry (LDA) in a turbulent bubbly flow to show that the classical $-5/3$ Kolmogorov energy spectrum exponent is progressively substituted by a $-8/3$ exponent with increasing gas fraction α. They proposed that the steeper spectrum originates from the immediate dissipation of bubble wakes. They also put forward arguments based on dimensional analysis that the energy spectrum exponent is -3 for pseudo-turbulence. From the definition of the bubblance parameter, one would expect different spectral scaling behavior depending on the energy input that is

more dominant. For b $\ll$ 1 the active-grid-induced turbulent fluctuations would be more dominant and hence the spectrum exponent would be close to $-5/3$ (Kolmogorov). When b $\gg$ 1, the bubble-induced fluctuations would be important and the exponent would be closer to -3 (see [16]) for a review). Recent experiments ([8]) have conclusively found that the energy spectrum exponent is close to -3 for the pseudo-turbulent case (b $= \infty$). Other experiments in the wake of a swarm of rising bubbles (b $= \infty$) also found a spectral exponent ~ -3 ([17]). Although a few early studies ([2, 12]) have reported a spectrum scaling of $-5/3$ for b $=\infty$, recent work have clearly established that the pseudo-turbulence spectrum scaling is close to -3 ([8, 11, 18]). In fact, the -3 spectrum scaling is found to be robust even if the bubble size is changed, or if higher viscosity liquids are used instead of water. The recent study by [11] suggests that the specific details of the hydrodynamic interactions among bubbles do not influence the way in which the pseudo-turbulent fluctuations are produced. The current understanding is that the bubble-induced turbulence mainly results from the bubble wakes. The importance of the bubble wakes on the -3 spectrum scaling has also been established using numerical simulations by comparing the spectrum scaling between point-like bubble simulations ([10]) and fully-resolved simulations of freely rising deformable bubbles ([22]), with the former one giving $-5/3$ due to the absence of wakes, and the latter fully-resolved simulations giving -3 as the spectral scaling exponent.

A new approach proposed by [20] is to decompose the total liquid fluctuations into two contributions: spatial and temporal parts. Experiments with rising bubbles can only measure the sum of the spatial and the temporal fluctuations; and the two contributions cannot be easily distinguished. However, experiments with a fixed array of spheres distributed randomly in a uniform flow have been able to separately study the two contributions ([20]). These experiments have suggested that the spatial contribution is dominant over the temporal part upto bubble Reynolds numbers ~ 1000. Recent numerical simulations have found that the spectra of both the spatial and temporal contributions result in a -3 scaling ([18]). In the present work, we add external turbulence using an active-grid to the system of rising bubbles by varying the b parameter. Previous work has mainly been concerned with the extreme values of the b parameter, i.e. either pseudo-turbulence (b $= \infty$) or single-phase turbulence (b $= 0$). Our focus in this paper is to study what happens in between these extremes b $= \infty$ and b $= 0$ as the energy spectrum scaling and the liquid velocity fluctuation statistics are not well known for large ranges of intermediate b. In this paper, we thus want to systematically analyze the flow as a function of the b parameter between the cases of single-phase turbulence (b $= 0$), turbulence with some bubbles ($0 < $ b < 5). The b parameter is varied over 2-3 orders of magnitude, namely from 0.01 to 5, and the pseudo turbulent case b $= \infty$ is also included.

In the next section, we describe the experimental setup, tools and methods used. This is followed by the results section where we describe our findings for the liquid velocity fluctuations and energy spectra. We provide an interpretation of our results in the discussion section and summarize our work.

2.2   Experiments

2.2.1   Experimental Setup

The experiments are carried out in the Twente Water Tunnel (TWT) facility, which is an 8 m-high vertical water tunnel (see Figure 2.1). The measurement section of the TWT (dimensions: $2m \times 0.45m \times 0.45m$) is made of transparent glass to provide optical access for flow visualization and measurements. We place the phase-sensitive CTA (hot-film) probe in the center of this measurement section, more details on this technique are discussed in the next section. An active-grid is used to generate nearly homogeneous and isotropic turbulent flow in the liquid phase and it is placed below the test section ([13, 15, 9]). Air bubbles are generated by blowing air through islands of capillary needles that are located below the measurement section. A U-tube setup mounted in the measurement section is used to measure the gas void fraction α (see [16, 8] for more details). The bubbles pass through the active-grid, rise through the measurement section and eventually escape through an open vent at the top of the TWT. The liquid mean flow is driven by a pump which recirculates the water throughout the TWT. The bubbles rise along with the upward mean flow in the measurement section; in other words, the system is a co-flowing turbulent upward bubbly flow.

In the present experiments, the b parameter:

$$b = \frac{1}{2} \frac{\alpha U_r^2}{u_0'^2} \qquad (2.2)$$

is varied by changing: (i) the volume flow rate of air (i.e. equivalent to changing the gas void fraction α) through the capillary islands, (ii) the magnitude of the mean flow speed of water in the upward direction (to effectively change the turbulence intensity $u_0'^2$). In equation 2.1, U_r is the typical bubble rise velocity (in still water), and for both set 1 and set 2 we assume $U_r \approx 23$ cm s^{-1} ([1]).

We vary the bubble diameter by changing the inner diameter of the capillary needles in the bubble generating islands. Air bubbles of diameter 3-5 mm and 2-4 mm are produced using capillary needles of inner diameter 500 μm and 120 μm, respectively. We classify our experiments into two sets based on the bubble diameter - experiments with bubbles of diameter 3-5 mm belong to set 1, and experiments with bubbles of diameter 2-4 mm are referred to as set 2 (see Table 2.1). We obtain b parameter values from ∞ to 0 by varying the void fraction (2 to 0%) and the mean flow velocity (0 to 60 cm s^{-1}). Table 2.1 lists all the different parameters varied in the present experiments.
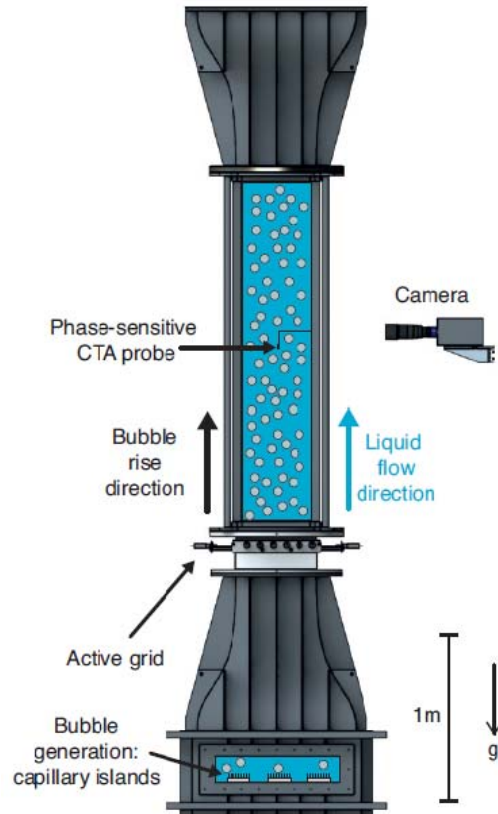
Figure 2.1: The Twente Water Tunnel (TWT) facility. A vertical multiphase water tunnel where homogeneous and isotropic turbulence is generated by an active-grid. Air is blown through capillary islands located below the measurement section to generate bubbles. The bubble rise direction and liquid flow are both in the upward direction, and the phase-sensitive CTA probe measures the liquid velocity fluctuations.

Set 1				Set 2			
b	α	u'_0	U_l	b	α	u'_0	U_l
	%	cm s^{-1}	cm s^{-1}		%	cm s^{-1}	cm s^{-1}
∞	2	0	0	∞	2	0	0
∞	1.17	0	0	∞	1.5	0	0
4.13	1	0.8	10	∞	1	0	0
2.06	0.5	0.8	10	∞	0.8	0	0
1.03	1	1.6	20	∞	0.5	0	0
0.78	0.75	1.6	20	4.13	1	0.8	10
0.52	0.5	1.6	20	2.06	0.5	0.8	10
0.17	0.67	3.2	40	1.03	1	1.6	20
0.08	0.3	3.2	40	0.78	0.75	1.6	20
0.03	0.17	4	50	0.52	0.5	1.6	20
0.01	0.083	4.8	60	0.37	0.8	2.4	30
0	0	2.4	30	0.23	0.5	2.4	30
				0.21	0.2	1.6	20
				0.15	0.6	3.2	40
				0.08	0.3	3.2	40
				0.03	0.2	4	50
				0	0	2.4	30

Table 2.1. Experimental parameters, set 1: 3-5 mm bubbles, set 2: 2-4 mm
bubbles.

The turbulent flow properties (e.g. $u_0'^2$) are characterized by combined CTA
- LDA (Laser Doppler Anemometry) measurements of only the liquid phase at
different mean flow speeds (for details see [9]). In order to visualize the flow,
a Photron-PCI 1024 high-speed camera was focused on a vertical plane at the
center of the measurement section. We acquired two-dimensional images of each
experiment using the camera (at $1000Hz$) and some of these snapshots are shown
in Figure 2.2. The b $= \infty$ experiments are shown in Figure 2.2(a) and (b) where the
gas void fractions are $\alpha = 2\%$ and 1%, respectively. The dense nature of the flow
at such void fractions is evident: the flow is opaque and the phase-sensitive CTA
probe is barely visible. As we proceed to look at the other cases in Figure 2.2(c)-
(f), ∞ decreases, and the liquid mean flow speeds (U_l) increase, corresponding to
a decrease in the b parameter from 1 to 0:03. In our experiments, the bubbles
must pass through the active-grid, which consists of randomly oscillating steel flaps
($\approx$ few rotations per second) to generate the required turbulence. At any given
instant of time, the active grid is 50% transparent (open) to the flow. Hence,
the bubbles face a slight obstruction and sometimes interact with the steel flaps.
The obstruction has a local effect which is negligible when considering the overall
flow, and the CTA probe is located sufficiently far away ($\approx 1m$) from the active-
grid. The bubble-flap interaction, however, causes fragmentation of the bubbles and
results in a decrease of the diameter of the bubbles. This bubble diameter decrease
becomes apparent at higher liquid mean flow speeds (U_l), as seen in Figure 2.2(c)-
(f). We obtain a quantitative measurement of the bubble diameter using the images

acquired (Figure 2.2) from the individual experiments. The bubbles highly deform over time, and given the dense nature (high α) of the flows, there is currently no reliable automated image processing algorithm available to accurately determine the bubble diameter. Hence, we had to resort to a manual procedure - where individual bubble boundaries are marked using mouse-clicks in the open-source *ImageJ* software. An ellipse is fitted to the deformed bubble boundaries, and the equivalent bubble diameter is calculated as: db $= (d_l^2 d_s)^{-\frac{1}{3}}$, where d_l and d_s are the long and short axes of the ellipsoidal bubble. In each experiment, we measure the diameters of $\approx$ 50 - 100 bubble samples, and then take the mean value of the distribution to be the equivalent diameter of the bubble. In Figure 2.3 we observe that the bubble diameter decreases with a decrease in the b parameter (increasing liquid mean flow speeds). The decrease in the bubble diameters at higher liquid mean flow speeds is mainly due to the fragmentation of the bubbles (as described above) (also see [15]). Here, the error bars represent the standard deviation of the measured distribution of bubble diameters. At high mean flow speeds, air is entrained from an open vent at the top of the TWT because of oscillations of the free-surface exposed to the atmosphere. The entrained air unavoidably results in microbubbles which are fed back into the measurement section and contaminate the flow. These entrained micro-bubbles pose a problem at mean flow speeds higher than 30 cm s^{-1}, and are visible (as very small bubbles) in Figure 2.2(e) and (f). It is necessary to account for these micro-bubbles in the data analysis, and this issue will be discussed further below. The present experiments in the pseudo-turbulence regime (b $= \infty$) for set 1, are essentially the same as the measurements carried out in [8], and serve as a reference case for the data analysis and results. For this case of freely rising bubbles in a quiescent liquid, the bubble-based Reynolds number $Re = d_b U_r / \nu \approx 1000$ ([8]), where ν is the kinematic viscosity of water $(1 \times 10^{-6} m^2 s^{=1})$.

2.2.2 Phase-sensitive Constant Temperature Anemometry

Hot-film anemometry is a preferred technique in single-phase turbulent flows, but its application in bubbly flows is not straightforward. Since it is an intrusive technique, bubble-probe interactions result in disturbances in the hot-film time series voltage signal. Various methods have been developed in the past to remove these 'bubbly spikes' ([24, 16, 7]), so as to exclusively analyze only the liquid fluctuation segments measured by the hot-film probe. For example, a threshold method was used by [24] and [7]) and a pattern-recognition method was used by [16]. These methods essentially come up with an indicator function that labels the gas and liquid phase separately. However, a much better approach to eliminate the bubbly spikes from the CTA signal is to measure the indicator function in-situ during the experiments. This can be done by attaching optic fibers with a diameter of $\sim$ 100 μm close to the hot-film probe (at a distance $\sim$ 1 mm) to detect the gas phase. Light is continuously passed through the optic fiber, and when a bubble collides with the probe, the change in refractive index of the gas phase results in a signal change. This technique, called the phase-sensitive Constant Temperature Anemometry (CTA)
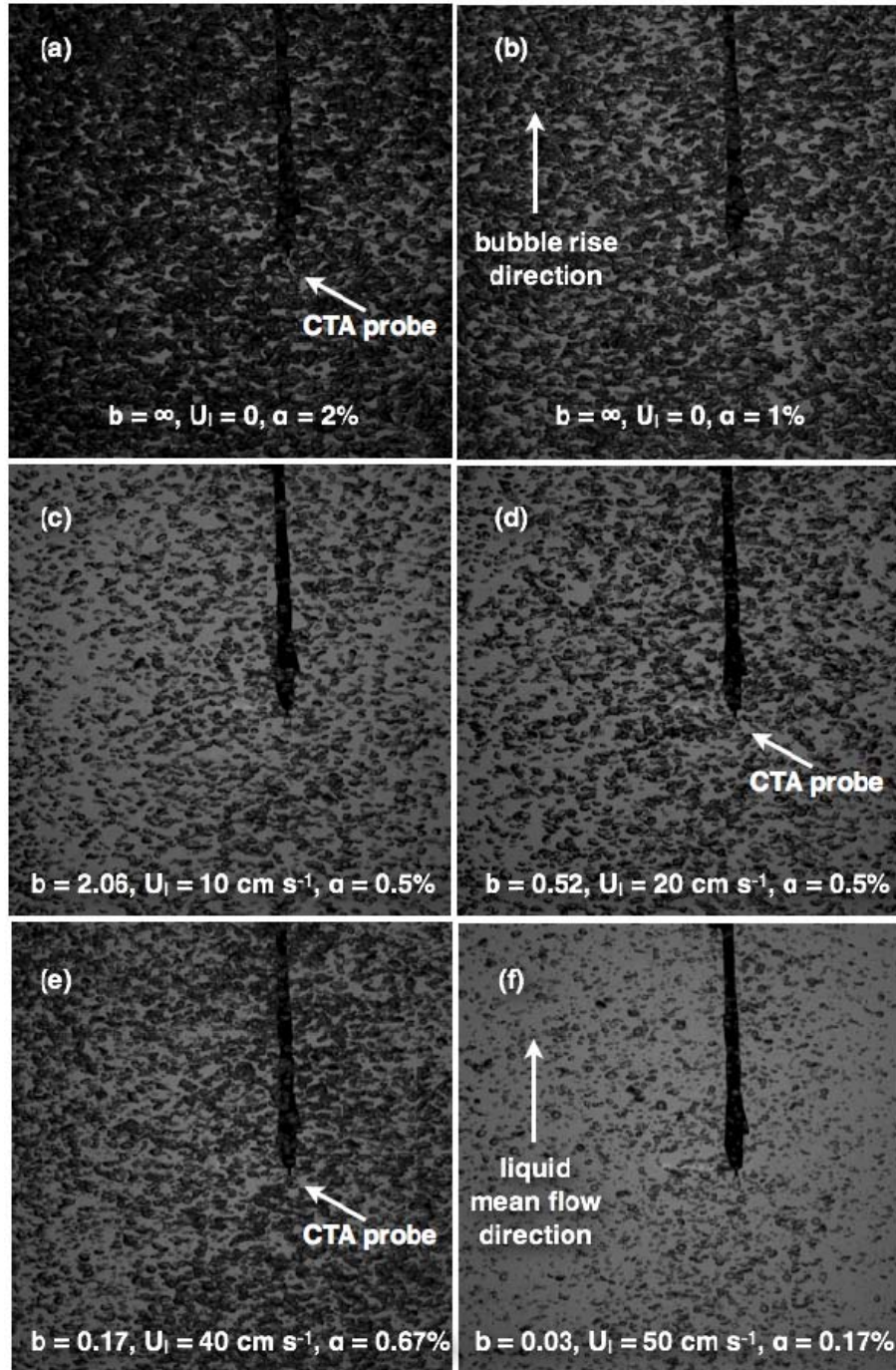
Figure 2.2: Snapshots from the experiments (set 1, see Table 2.1) at different conditions.
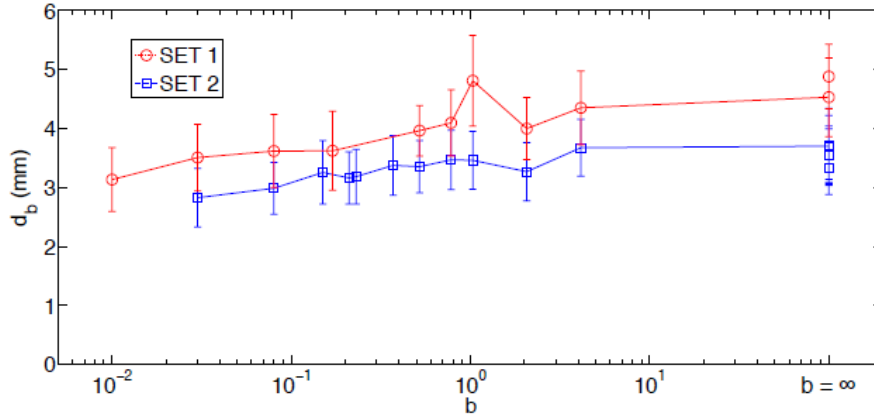
Figure 2.3: Bubble diameters versus the b parameter. The error bars are estimated based on the standard deviations.

was developed by [23] and is used in [8] and [11]. This method can be used to directly detect and remove the bubbly spikes in the hot-film signal. In this work, we follow almost the same experimental procedure and analysis as in [8], but the important difference here is that we vary the b parameter over a wide range to cover the regimes between pseudo-turbulence (b = ∞) and single-phase turbulent flow (b = 0). The phase indicator function obtained using information from the optic fiber signal labels the liquid fluctuations and bubble collisions separately. This is used to remove the bubbly spikes and separate the segments containing only liquid fluctuations from the time series signal for further analysis. The power spectrum was calculated for each segment of liquid fluctuation and averaged to obtain the spectrum for a particular case of b. The phase-sensitive CTA probe is calibrated by simultaneous measurement of absolute velocities of the single-phase using a DANTEC Laser Doppler Anemometry (LDA) setup (as in [15, 9]). The standard King's law fit is used for the voltage-velocity data. The acquisition rate was 10 kHz and the measurements were carried out for a duration of 1 hour in each case. The phase-sensitive CTA technique works very well for pseudo-turbulent bubbly flows where the bubble diameters are in the range $\sim$ 2-5 mm. However, when micro-bubbles collide with the CTA probe, the optic fibers will not be able to register the collision. The reasons for this are two-fold: (i) the micro-bubbles are small in size ($\leq$ 300 μm diameter), and (ii) the separation distance between the CTA probe and the optical fibers is larger ($\sim$ 1 mm) than the micro-bubble size. As we mentioned before, micro-bubbles cause a contamination in the present experiments when the mean flow speeds exceed 30 cm s^{-1}. In these experiments, we inevitably use a threshold method to remove the micro-bubble collisions, in addition to the phase information obtained from the optic fibers. Further, to keep the data analysis consistent, the combination of the optical fibers and the threshold method is also used in all the experiments except pseudo-turbulence, where only the optical fibers

are used.

2.3   Results and Discussion

2.3.1   Liquid velocity statistics

The liquid velocity time-series signal was measured using the phase-sensitive CTA technique at different b parameter values. We now consider the statistics of these liquid velocity fluctuations using the separated segments of the signal which are free from the bubble collisions. In Figure 2.4, we present the normalized liquid velocity probability density functions (PDFs) for the different values of b covered in the present work, including both set 1 and set 2 experiments (see Table 2.1). The liquid velocity PDF for single-phase turbulent liquid (b = 0) at a mean flow of 30 cm s^{-1} (Taylor Reynolds numbers Re_λ= 170) (black dots) closely follows Gaussian statistics. This single-phase result serves as the reference case. The liquid velocity PDFs for the cases with bubbles (b > 0) are asymmetric and show a deviation from Gaussian behavior. The positive tails of the PDFs show higher probability compared to the Gaussian profile. This is probably because of flow entrainment in the wake of the rising bubbles, which leads to a larger probability of upward fluctuations ([16, 17]). The velocity PDFs for the two pseudo-turbulence cases in the set 1 experiments (b = ∞; α = 2; 1.17 %) show higher upward fluctuations and almost collapse (Figure 2.4(a)). In the pseudo-turbulent cases (b = ∞) of the set 2 experiments, the velocity PDFs also show a clear deviation from the Gaussian distribution, with more upward fluctuations (Figure 2.4(b)). Within these experiments (b = ∞), for different void fractions (α = 2%; 1.5%;1%; 0.8%; 0.5%) there is no clear trend, but all the cases show an asymmetric profile compared to the purely liquid phase (b = 0). As the b parameter decreases to b = 4.13 - 1.03 in the set 1 experiments (Figure 2.4(c)), we see both increases and decreases in the positive tails compared to the pseudo-turbulent cases. In the set 2 experiments, at b = 4.13 - 1.03 (Figure 2.4(d)), the results are comparable to the pseudoturbulence cases (Figure 2.4(b)). In Figure 2.4(e), for the set 1 experiments, the b parameter values are in the range b = 0.78 - 0.01. Although we do not observe a clear trend on the dependence of the PDF shape on the b parameter, it is clear that the positive tails of the PDFs show more upward fluctuations compared to the Gaussian profile, as far as bubbles are present in the system. The velocity PDFs corresponding to the set 2 experiments with b parameter values 0.78 - 0.03 (Figure 2.4(f)) in general show a reasonable collapse (except the b = 0.21 case). Similar to the set 1 results, the upward fluctuations of the liquid velocity PDFs in general decrease as the b parameter values decrease and start approaching the purely liquid phase (b = 0). All the bubbly flow cases (b > 0) show a deviation from the Gaussian profile, and are asymmetric with the positive tails showing a higher probability of upward fluctuations. We further examine the statistics of the liquid velocity fluctuations for different values of the b parameter. In Figure 2.5, we plot the standard deviation values of the liquid fluctuations for each case of the b parameter. In Figure 2.5, as we
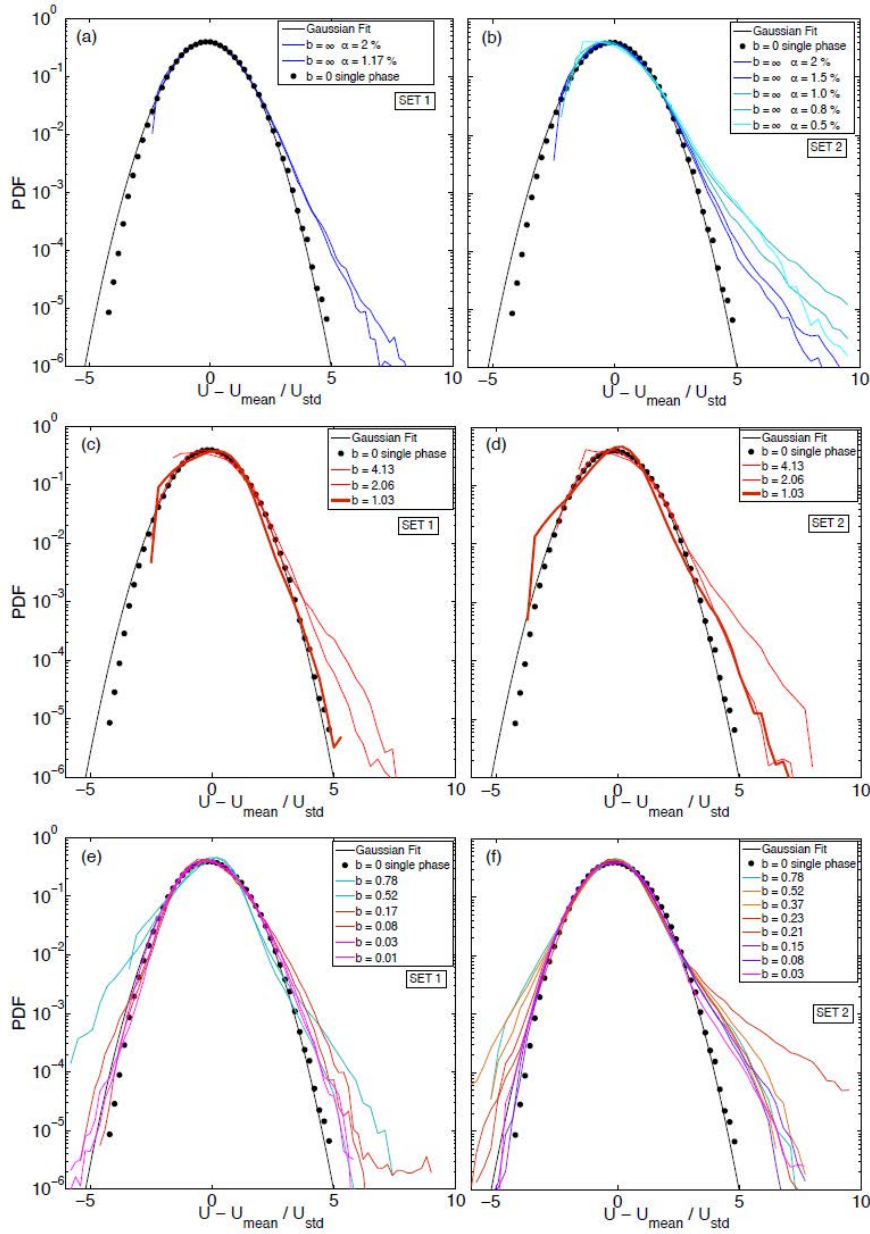
Figure 2.4: The liquid velocity PDFs for different b, left panel: set 1, right panel: set 2. (a, b) represent $b = 0, \infty$, (c, d) $b = 0$ and > 1, (e,f) $b = 0$ and < 1. All the bubbly flow cases show deviations from the Gaussian profile with enhanced probability of upward fluctuations.
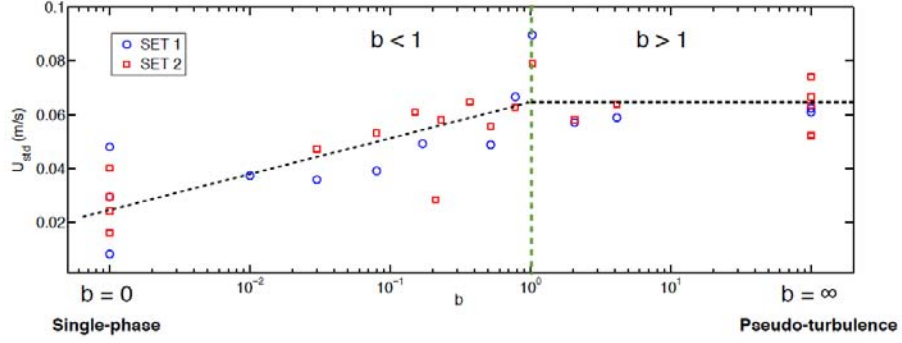
Figure 2.5: Liquid velocity fluctuation statistics at different b parameter values. For $b < 1$, the net liquid fluctuations weakly increase with the b parameter. For $b > 1$, there is no clear dependence on the b parameter.

move towards the left (b → 0), the energy induced by the liquid mean flow starts to become dominant, and as we move towards the right (b → ∞), the energy induced by the bubbles is dominant. The net liquid fluctuations in the system, measured by the standard deviation of the liquid fluctuations, slightly increase with increase in the b parameter up to b ≈ 1 (as indicated in Figure 2.5), and then saturate. When b < 1, the externally-induced turbulent energy (resulting from the active-grid) weakly decreases the net fluctuations with decrease in the b parameter. When b > 1, the bubble-induced kinetic energy dominates and there is no dependence of the fluctuations on the b parameter. This implies that adding the active-grid-induced external turbulence to a bubbly flow does not significantly change the total liquid fluctuations. There is a reasonable agreement between the trends shown by the two datasets (set 1 and set 2) in the present study. We discuss results on the velocity PDFs and energy spectra at three regimes based on the classification in Figure 2.5: the pseudo-turbulence regime (b = 1), the mixed regime b > 1 (b ∼ $O(1)$), and the mixed regime approaching single-phase b < 1 (b ∼ $O(0.01, 0.1)$).

2.3.2 Energy Spectra

We will now focus on the turbulent energy spectrum of the liquid velocity fluctuations at the different regimes of b. The energy spectrum scaling is well-established for the standard cases of single-phase turbulence (b = 0): the classical Kolmogorov $-5/3$ scaling (apart from intermittency corrections, [14]), and for pseudo-turbulence (b = ∞): a -3 scaling ([5, 8, 22, 18, 11]). Here, we want to investigate how the spectrum scaling changes from pseudo-turbulence (-3) to single-phase turbulence ($-5/3$). The energy spectrum (Power Spectral Density, PSD) was calculated for individual segments of the liquid fluctuations (free from bubbly spikes) using the Welch method (using hamming windows) at fixed frequencies, and then averaged over all the liquid segments in the measurement to obtain the final result (as in [8]).
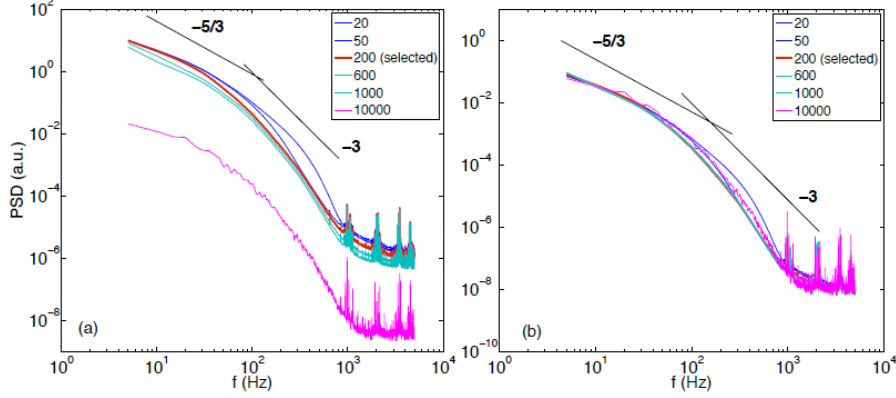
Figure 2.6: Minimum sample size criterion for the calculation of the energy spectrum, for the case $b = 0.23$ (set 2) (a) non-normalized spectra (b) normalized spectra. The different colored lines are the spectra obtained with various sample sizes, as shown in the legend. The normalized spectrum (b) does not change when the sample size is sufficiently long. A sample size of 200 is found to be optimal in the present work with the sampling frequency of 10 kHz.

The segments selected for the spectrum calculation must have a certain minimum length to properly resolve all the frequencies; segments that are too short will lack information on the large length-scales (low frequencies) and will simply add to the high frequency components of the spectrum (noise). We investigate the effect of varying this minimum sample size criterion on the spectrum for a selected case of b = 0.23 (set 2); the results are shown in Figure 2.6. We observe drastic changes in the spectra depending on the value of the minimum sample length. In Figure 2.6(a) we show the spectra directly obtained from the calculation. Both the amplitude and the scaling change; with a monotonic decrease in energy with increase in sample length. This is expected because when we increase the minimum sample length considered, we have fewer segments considered and the average energy decreases. In the extreme case of minimum sample length of 10000 data points ($\sim$ 1s), the spectrum looks noisy as it was averaged only over 80 segments. For the present data, we have selected an optimal minimum sample length of 200 data points ($\sim$ 0.02s), which nicely resolves all the frequencies (the spectrum is averaged over 14500 segments). In Figure 2.6(b), we show the same spectra after normalizing the area under the curve to be equal to unity. We observe that the selected value of 200 is an optimal value; the values (20, 50, 10000) show deviations in the scaling. In the sections that follow, we present results for the normalized spectra in all the cases of b parameter as it allows us to focus solely on changes in the scaling. The energy in the non-normalized spectra depends on the number of samples considered in the averaging, and this can differ in each experiment as it depends on the flow conditions; hence, we normalize the spectra. The spectra for different values of b

are shown in Figure 2.7.

The shown spectra are the calculated PSD (in arbitrary units) per frequency versus the frequency (in Hz), and they are normalized so that the area under the curve equals unity. The solid lines are drawn to aid comparison of the present results with the two 'standard' power law scalings (-3 and $-5/3$). We also show these spectra compensated with the $-5/3$ and -3 scaling in Figures 2.8(a),(b) and (c),(d) respectively. The single-phase turbulent spectrum is shown in all the cases and serves as a reference case. As expected, the single-phase spectrum (b = 0, black solid line) shows a good agreement with the Kolmogorov $-5/3$ scaling in the inertial range (at lower frequencies, large length scales), and rapidly drops in energy as we move towards the dissipative range (higher frequencies, smaller length scales). We first consider the bubbly spectra in the pseudo-turbulence regime (b = ∞) from the set 1 experiments (see Table 2.1) in Figure 2.7(a). These pseudo-turbulence cases, b = ∞, α = 2% and 1.17% nicely follow the -3 scaling, with a clear deviation from the single-phase spectrum, confirming previous results (e.g.[8, 18, 11]). It is believed that the -3 spectrum sub-range at intermediate length scales originates from the wakes of the rising bubbles. We mark the characteristic frequency of the freely rising bubbles (set 1): $f_{b1} \approx U_r/2\pi d_{b1} \approx 9 \simeq O(10)$ Hz, where, $U_r \simeq 23cm$ s^{-1} ([1]) is the bubble rise velocity in still water, and d_{b1} = 5-3 mm is the range of bubble diameters (see Figure 2.3). This frequency f_{b1} represents a transition (or cut-off) frequency where the bubbly spectra change slope from $-5/3$ (Kolmogorov) to -3 (pseudo-turbulence). The bubbly spectra follow the $-5/3$ (Kolmogorov) scaling till the transition frequency f_{b1}, beyond which they follow the -3 pseudo-turbulence scaling. In Figure 2.7(b), we compare these pseudo-turbulence results (set 1 experiments) to a different size distribution (set 2 experiments) of the bubbles (see Table 1). All of the b = ∞ cases in the set 2 experiments with α = 2, 1.5, 1, 0.8; 0.5%, nicely follow the -3 spectrum scaling beyond the transition frequency f_{b2} (also see the -3 compensated plot - Figure 2.8(d)). Here, the characteristic bubble frequency is $f_{b2} \approx U_r/2\pi d_{b2} \approx 12 \simeq O(10)$ Hz, where, $U_r \simeq 23cm$ s^{-1} ([1]) is the bubble rise velocity in still water, and d_{b2} = 4 - 2mm is the bubble diameter for the set 2 experiments (see Figure 2.3). These results once again confirm the typical pseudo-turbulence -3 energy spectrum scaling for freely rising bubbles. Hence, for length scales smaller than the bubble size ($f > f_b$), the turbulence induced by the bubble wakes results in a -3 scaling and for larger length scales ($f < f_b$), the classical Kolmogorov $-5/3$ scaling seems to hold. We now depart from the pseudo-turbulent case and get into mixed regimes which are in between pseudo-turbulence and single-phase. For b parameter values in the order of 1, i.e. for b > 1, the net fluctuations did not show a change when the b parameter changes from pseudo-turbulence (b = 1) to b $\sim O(1)$ (Figure 2.5), then the question is whether there is a change in the spectra? The spectrum results for the set 1 experiments (b = 4.13, 2.06, 1.03) and set 2 experiments (b = 4.13, 2.06, 1.03) are shown in Figure 2.7(c) and (d) respectively. We observe that the spectra do not change significantly as compared to the pseudo-turbulent case. Although there is a very slight energy decrease at frequencies around 100 Hz compared the pseudo-turbulent cases, the -3 scaling still holds. At b parameter values less than 1 (b < 1), we have
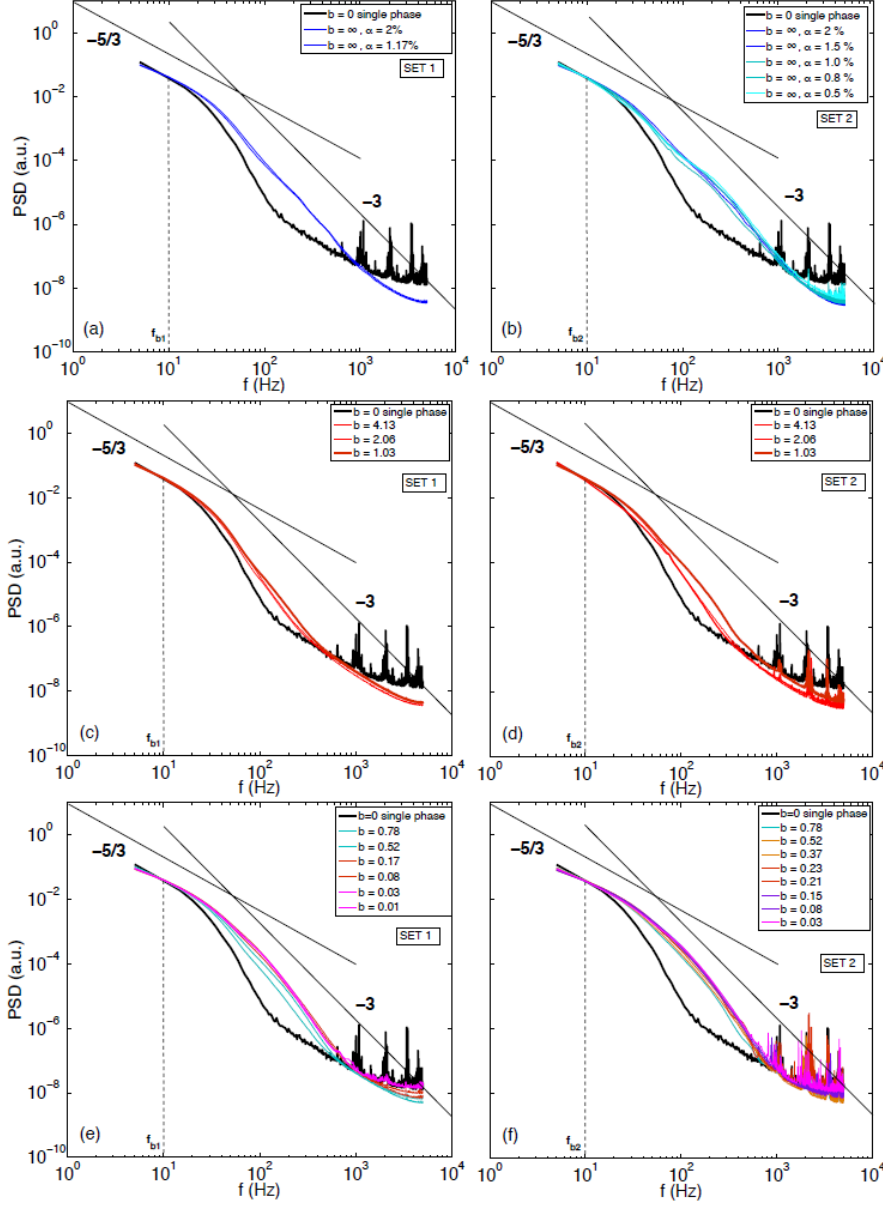
Figure 2.7: The normalized energy spectra at different b, left panel: set 1, right panel: set 2. (a, b) represent $b = 0$, ∞, (c, d) $b = 0$ and > 1, (e,f) $b = 0$ and < 1. All the bubbly flow cases show deviation from the $-5/3$ Kolmogorov single-phase spectrum beyond the transition frequency (at 10 Hz as indicated with the dotted line), and reasonably follow the -3 scaling.

previously seen (in Figure 2.5) that the net liquid velocity fluctuations show a weak decrease with decreasing b parameter value. In this regime, the surrounding liquid turbulence starts to have a dominant contribution. Hence, it is interesting to study how the spectra eventually approach the single-phase scaling behavior. We now look at the spectral results for b parameter values in the order of $\sim O(0.01, 0.1)$. Figure 2.7(e) shows the spectrum results for the set 1 experiments with b parameter values b = 0.01 - 0.78. Surprisingly, we observe that the -3 scaling is still followed in all the cases beyond the transition frequency f_{b1}. We can also observe a very slight increase in energy at the intermediate scales (around frequencies $\sim$ 100 Hz) as the b parameter decreases from b = 0.78 to b = 0.01, but the -3 scaling does not change much. In the set 2 experiments (Figure 2.7(f)), we cover more cases of the b parameter, b = 0.78 to 0.03, and find that the results are very similar to the set 1 experiments (Figure 2.7(e)). Once again, there is a gradual energy increase at the intermediate scales as b parameter decreases from b = 0.78 to b = 0.03, but the -3 scaling is followed nicely. In the cases at low b $\sim O(0.01)$, the active-grid-induced turbulence dominates the flow, but remarkably the spectra still show a reasonable -3 subrange scaling. This finding suggests that even a small 'contribution' of turbulent flow by bubble wakes is sufficient to modify the spectral properties, due to the long lifetime of the bubble wakes. The two experimental sets with different bubble diameters (set 1 and set 2) have revealed essentially similar results and trends.

2.4   Discussion and Summary

We have systematically varied the bubblance parameter from b = ∞ to b = 0.01, and studied in detail the liquid velocity PDFs and energy spectra. The liquid velocity PDFs for the bubbly cases (b > 0) show asymmetry, and more upward fluctuations compared to a Gaussian profile. When b < 1, the net liquid fluctuations reveal a weak dependence with the b parameter; a slight decrease in the fluctuations with decrease in b. We then looked at the effect of varying the bubblance parameter on the energy spectrum scaling. We have seen in Figure 2.7 that the energy spectra for all the cases (both set 1 and set 2) with bubblance parameter b > 0 follow the $-5/3$ Kolmogorov spectrum scaling at the large length-scales (see Figure 2.8(a),(b)). Beyond the transition frequency, all the bubbly spectra roughly exhibit the -3 subrange scaling (see Figure 2.8(c),(d)), which has been associated with the bubble wakes. In our experiments, we have added active-grid-induced turbulence to the configuration of rising bubbles to change the b parameter. The active-grid-induced turbulence has a weak influence on the velocity fluctuations, but why does not it have an influence on the turbulent energy spectra? We will look for clues to answer this question by probing deeper into the physics of bubbly flows. Risso and co-workers proposed that multi-body wake-interaction mechanisms can be studied by decomposing the velocity fluctuations into spatial and temporal contributions ([20, 21, 18]). Denoting the spatial averaging by brackets, and time averaging by an overbar, the total variance of the velocity can be decomposed into
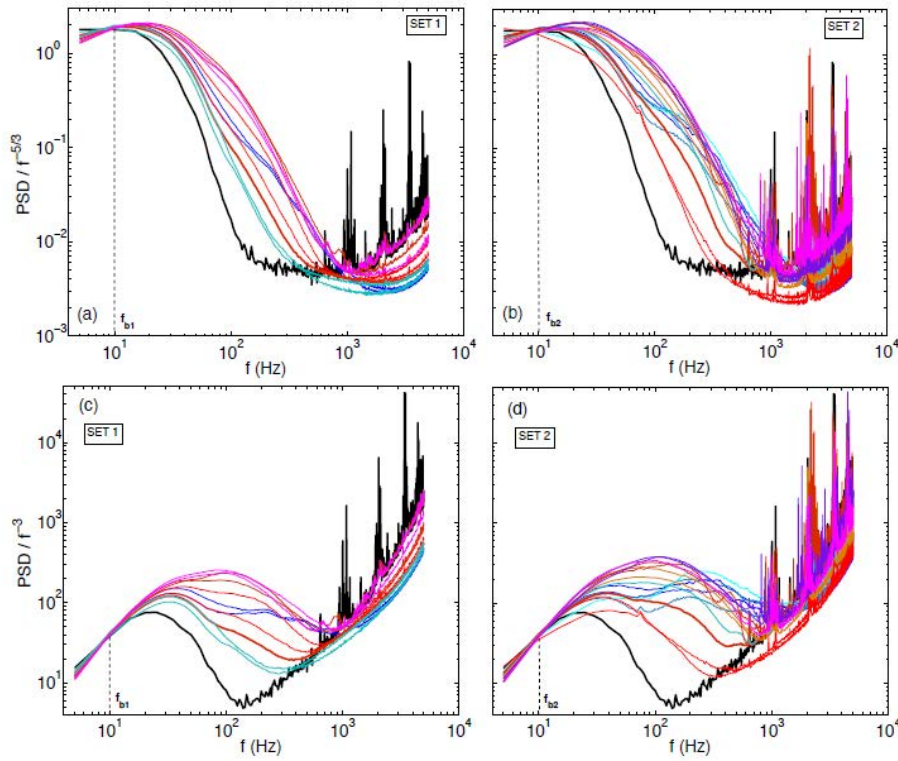
Figure 2.8: The compensated energy spectra at different b. left panel: set 1, right panel: set 2. (a,b) spectra compensated with $-5/3$, (c,d) spectra compensated with -3. The thick black lines indicate the single phase case. The colors for the bubbly flow cases correspond to the scheme in Fig. 2.7. As observed in (c,d), all the bubbly flow cases roughly exhibit the -3 scaling.

two contributions:

$$\langle u^2 \rangle = \langle \bar{u}^2 \rangle + \langle u^{'2} \rangle \qquad (2.3)$$

The first contribution $\langle \bar{u}^2 \rangle$ is associated with the spatial variations of the time averaged velocity. This spatial contribution is characterized by the random spatial distribution of the bubbles, and is not influenced by turbulence. The second contribution $\langle u^{'2} \rangle$ is related to temporal fluctuations, and changes with the turbulence intensity. It is evident that the spatial and temporal contributions correspond to different physical mechanisms. Although it would be beneficial to decompose their separate contributions, this is currently not possible in the present experiments because the bubbles do not rise at constant velocity and move relative to each other. However, such a decomposition was accomplished using experimental investigations of an array of fixed spheres ([20]). They found that the spatial contribution is more dominant than the temporal one in the vertical direction (see Figure 5 in [20]) up to Reynolds numbers ~ 1000. It was deduced that the spatial contributions are mainly responsible for the enhancement of the wake decay, in other words, the -3 subrange scaling. Risso ([21]) theoretically showed that the superposition of independent random bubble disturbances may generate a continuous spectrum with a -3 subrange. Recently ([18]) numerically found that both the spatial and temporal contributions exhibited the -3 subrange, which might be an explanation for why it is always observed in experiments. In our experiments, we vary the active-grid-induced turbulence intensity (and b parameter) by changing the mean flow speed. According to the discussion above, this means that we mainly change the temporal contributions, while the spatial contribution dominates in the explored parameter regime (at bubble Reynolds numbers ~ 1000). In our experiments, it is not possible to control (or vary) the dominant spatial contribution. This is probably why we see the robust -3 subrange for turbulent bubbly flow in a wide variety of conditions (b > 0) over 2-3 orders magnitude change in the b parameter. Hence, the -3 spectrum scaling seems to be a generic feature in turbulent bubbly flow. Remarkably, the -3 spectrum scaling is followed even at very small b parameter values (~ 0.01); i.e. when the void fraction is as low as 0.1%. Hence, the bubbles are able to modify the spectra very efficiently, even though they are present in small numbers, due to the long lifetime of their wakes. However, at extremely small bubble concentrations $\alpha \ll 0.1\%$ and b $\ll 0.01$ the Kolmogorov-like single-phase spectrum should be recovered, but we have no hint when this will happen. It would be relevant to find this transition in future work. The bubble concentration of the transition regime may be so small that optical methods like laser doppler anemometry (LDA) or particle image velocimetry (PIV) may become applicable, and even numerical approaches with fully-resolved wakes might be suitable for this purpose. In any case, it will be interesting to test until what limit of the b parameter the -3 scaling still holds.

Bibliography

[1] Clift, R., & Grace, J. R. & Weber, M. E. 1978, Bubbles, Drops and Particles, Academic, New York.

[2] Cui, Z., & Fan, L. S. 2004, Turbulence energy distributions in bubbling gas-liquid and gas-liquid-solid flow systems, Chem. Eng. Sci. 59, 1755-1766.

[3] Deckwer, B. D. 1992, Bubble Column Reactors, Wiley, 1st edn.

[4] Ern, P. & Risso, F. & Fabre, D. & Magnaudet, J. 2012, Wake-induced oscillatory paths of freely rising or falling bodies, Ann. Rev. Fluid Mech. 44, 97-121.

[5] Lance, M., & Bataille, J. 1991, Turbulence in the liquid phase of a uniform bubbly water-air flow, J. Fluid Mech. 222, 95-118.

[6] Magnaudet, J. & Eames, I. 2000, The Motion of High-Reynolds-Number Bubbles in Inhomogeneous Flows, Ann. Rev. Fluid Mech. 32, 659-708.

[7] Martínez Mercado, J., Palacios Morales, C. & Zenit, R. 2007, Measurements of pseudoturbulence intensity in monodispersed bubbly liquids for 10<Re<500 Phys. Fluids 19, 103302.

[8] Martínez Mercado, J., Chehata, D., van Gils, D. P. M., Sun, C., & Lohse, D. 2010, On bubble clustering and energy spectra in pseudo-turbulence J. Fluid Mech. 650, 287-306.

[9] Martínez Mercado, J., Prakash, V. N., Tagawa, Y., Sun, C. & Lohse, D. 2012, Lagrangian statistics of light particles in turbulence Phys. Fluids 24, 055106.

[10] Mazzitelli, I., & Lohse, D. 2009, Evolution of energy in flow driven by rising bubbles, Phys. Rev. E. 79, 066317.

[11] Méndez-Díaz, S., Serrano-García, J. C., Zenit, R., and Hernández-Cordero, J. A. 2013, Power spectral distributions of pseudo-turbulent bubbly flows, Phys. Fluids 25, 043303.

[12] Mudde, R. F., Groen, J. S. & van der Akker, H. E. A. 1997, Liquid velocity field in a bubble column: LDA experiments, Chem. Eng. Science 52, 4217.

[13] Poorte, R. E. G. & Biesheuvel, A. 2002, Experiments on the motion of gas bubbles in turbulence generated by an active grid, J. Fluid Mech. 461, 127.

[14] Pope, S. B. 2000, Turbulent flows Cambridge University Press.

[15] Prakash, V. N., Tagawa, Y., Calzavarini, E., Martínez Mercado, J., Toschi, F., Lohse, D., & Sun, C. 2012, How gravity and size affect the acceleration statistics of bubbles in turbulence New J. Phys. 14, 105017.

[16] Rensen, J., Luther, S. & Lohse, D. 2005, The effects of bubbles on developed turbulence,J. Fluid Mech. 538, 153-187.

[17] Riboux, G., Risso, F. & Legendre, D. 2010, Experimental characterization of the agitation generated by bubbles rising at high Reynolds number J. Fluid Mech. 643, 509-539.

[18] Riboux,G., Legendre, D. and Risso, F. 2013, A model of bubble-induced turbulence based on large-scale wake interactions J. Fluid Mech. 719, 362-287.

[19] Risso, F. & Ellingsen, K. 2002, Velocity fluctuations in a homogeneous dilute dispersion of high-Reynolds-number rising bubbles J. Fluid Mech. 453, 395-410.

[20] Risso, F., Roig, V., Amoura, Z., Riboux, G. & Billet, A. M. 2008, Wake attenuation in large Reynolds number dispersed two-phase flows Phil. Trans. R. Soc. A. 366, 2177-2190.

[21] Risso, F. 2011, Theoretical model for k-3 spectra in dispersed multiphase flows. Phys. Fluids 23, 011701.

[22] Roghair, I., Martínez Mercado, J., Van Sint Annaland, M., Kuipers, J. A. M., Sun, C. & Lohse, D. 2011, Energy spectra and bubble velocity distributions in pseudo-turbulence:numerical simulations vs. experiments, Int. J. Multi. Flow 37, 1-6.

[23] van den Berg, T. H., Wormgoor, W. D., Luther, S. and Lohse, D. 2011, Phase-Sensitive Constant Temperature Anemometry Macromol. Mater. Eng. 296, 230-237.

[24] Zenit, R., Koch, D. L. & Sangani, A. S. 2001, Measurements of the average properties of a suspension of bubbles rising in a vertical channel, J. Fluid Mech. 429, 307-342.

3

Bubble Deformation and Breakup
by the Action of a Turbulent Flow†

Abstract

In the present work the deformation and breakup dynamics of single bubbles in
an isotropic homogeneous turbulent environment have been experimentally inves-
tigated. The turbulent intensities generated in this experiment are in the same
order of magnitude as those observed in stirred tanks or in turbulent channels com-
monly involve in bubble breakup processes. The present study aims to describe
some fundamental aspects of the bubbles response under certain critical conditions
which can lead to the breakup. Experimental measurements of the velocity field
and deformation history of individual bubbles were carried out simultaneously. The
bubble size used in the experiments was 3.1 mm in average. A fluctuating behav-
ior was observed on the bubble deformation owing to the competition between the
dominant forces involve in the process; however, we can determine that the main
contribution to the bubble breakage is due to the large gradients of turbulent ve-
locities and their intermittent presence. We analyze solely the area around the
bubble in the knowledge that only the velocity field near the bubble surface will
cause strong deformations. The interrogation areas used in this study were around
two times the bubble diameter. A mechanism of internal flow redistribution within
the bubbles was identified. This can be inferred by the existence of fluctuations in
the dynamic pressure owing to the intermittent presence of fluctuating velocities
around the bubbles, in this way the bubbles breakup when try to recover their
original shape.

3.1   Introduction

Many natural and engineering processes concern mass and heat transfer between two or more fluids. Some these examples comprise gas transfer in rivers, lakes or oceans or the atmosphere for the case of contaminant dispersion, among others [1, 2, 3, 4, 5]. In industry, turbulent two-phase flows are common such as the case for biological reactors or stirred tanks [6, 21]. In majority of these situations, both phases are in turbulent regime and multiple turbulence-bubble interactions occur. One of the most important features in these flows is the bubble breakage which can change the overall response of the flow. Bubble breakage is a complex phenomena that depends on the bubble sizes, the degree of turbulent intensity, turbulent scales, among others. A better knowledge of turbulent two-phase flows is crucial for diverse applications. The concept of isotropic homogeneous turbulence has proved to be particularly useful for develop of statistical theories in turbulence. Many researchers are still using it as a powerful model to understand the fundamental mechanisms in more complex turbulent flows. The simpler environment that the isotropic turbulence offers makes it possible to address such situations, both numerically and experimentally. Meanwhile the direct numerical simulations *(DNS)* can provides in some sense an exact and detailed description of the turbulent phenomena, but the experiments still remains without an exact solution in the range of the large Reynolds numbers. Numerous experiments have been proposed in the literature to produce homogeneous turbulent flows such as possible in an ideal situations [8, 9, 10, 11, 12].

Previously, most of the research has focused on the analysis the bubble-turbulence interaction from the point of view of the turbulent spectra, if this is damped or enhanced. In recent years an increased interest in the bubble breakage process in a turbulent environment has appeared. In those studies attention is centered to identify the main forces acting on the bubbles' surfaces [13, 14, 15]. Such is the case of the work of Risso & Fabre [16]. They identified two main breakup mechanisms, the first one occurs due to the direct interaction of a single energetic eddy and a deformable bubble, the second one correspond to a resonant mechanism, in this one the breakup take place owing to the cumulative effect of a succession of low energetic eddies impacting on the bubbles' surface. They note that the second mechanism could occur if the resident time of the bubble into the turbulent flow is large enough and also recognize a critical Weber number. In previous studies most of the researchers have taken images of bubbles and drops breakups in different turbulent environments mainly in turbulent pipes [17, 18, 19, 20, 21]. In such investigations they analyze the breakage process taken photographs using high-speed cameras. In those approaches various breaking steps were observed, they have in common different deformation forms as the oscillation, dumbbell and pinch off patterns. In some cases this oscillations are associated with ripples on the bubble surfaces. Following the Kolmogorov theory of turbulent breakage of particles, where is stated that the breakup process is defined by a critical Weber number We_{crit} [16, 22]. This Weber number it is important to quantify the turbulent kinetic energy and the surface tension forces. In a general approach is accepted that

the bubble breakup can also be presented at smaller critical Weber numbers, this could be the case when the bubbles deformation is large enough.

On the other hand, most of the research at this moment has been done analyzing bubbles or droplets breakage in an average isotropic turbulent flow statistically stationary but to our knowledge the direct effect of the velocity fluctuations on the bubbles' surfaces never have been measured and taken into account in the past. These are some of the reasons for which in this study, we use an experimental setup to generate an isotropic turbulent flow to investigate the history of deformation and the breakup of bubbles. This article summarizes the findings of our experimental study on the bubbles' breakup into a turbulent isotropic flow. The aim of this work is to visualize the bubble's behavior into a low Reynolds number turbulent flow to identify the influence of the structural characteristics of the turbulent flow on the deformation of individual bubbles and characterize the main mechanisms which initiate the breaking process. In the first section the experimental methods are described in which the experimental device is depicted followed by the description of the turbulent environment that was characterized by the particle image velocimetry technique (PIV) and the determination of the area of interest is shown, also the image processing procedure using high-speed video images is presented. In the next section the main results are displayed and finally the last section is dedicated to the concluding comments.

3.2 Experimental Methods

The experimental setup used is depicted in Fig. 1. The experiment consist of an acrylic rectangular container, with six pumps (three at each side of the tank) which drives the fluid from the bottom of the container and is injected to the center of the tank through flexible pipes provided with nozzles of 0.95 *cm* in diameter. A detailed description of the experimental device can be read in [25, 26]. The bubbles were injected to the container through a capillary tube achieving a bubble size of 3.0 *mm* in equivalent diameter. The measurements were taken simultaneously with the PIV technique with high temporal resolution and a high speed camera to acquire the bubble shape. This camera was synchronized to the PIV system.

3.2.1 Characterization of the Flow Field

Flow field measurement were carried out using a time resolved PIV system. The injection velocity was set by means of an electronic control to avoid an intermittent response of the pumps. The velocity field generated into the chamber was fully characterized. These results are showed bellow (see Table 3.1) and the flow field was found to be closely isotropic. The flow is characterized by high turbulent levels with almost zero-mean flow, and statistic values of skewness and kurtosis close to a Gaussian distribution ($S=$ 0.16, $K =$2.75), with an isotropic ratio nearly to one for this experimental condition (Fig. 2).
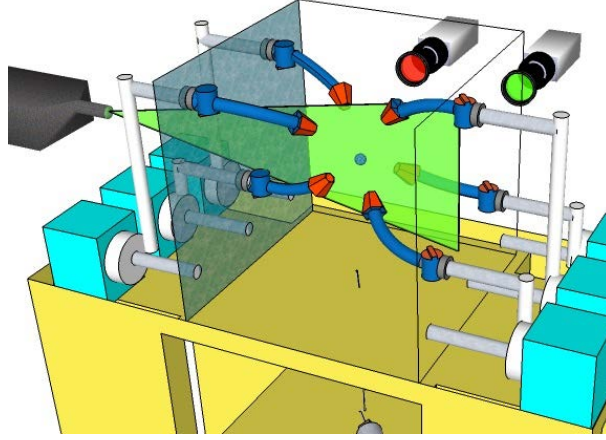
Figure 3.1: Schematic diagram of the experimental apparatus and the PIV system. The PIV camera was provided with a $680nm$ optical filter to acquire the velocity fluid phase and avoid scattered light from the bubbles.

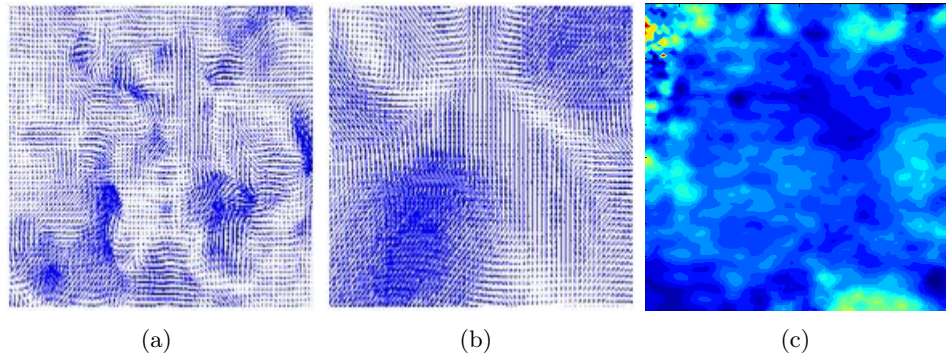(a)   (b)   (c)

Figure 3.2: Experimental measurements of the flow field. a) Instantaneous velocity field, b) Statistical velocity field, c) Isotropic ratio of fluctuating velocities.

$\langle U \rangle (ms^{-1})$	$\langle V \rangle (ms^{-1})$	$u'/\langle U \rangle$	$v'/\langle V \rangle$	u'/v'	Su	Sv	Ku	Kv
0.0073	0.009	6.58	5.55	0.97	0.20	0.12	2.68	2.79

Table 3.1: Statistic values of the average flow field.

3.2.2 Determination of the Interrogation Area

The area of interest over which the velocity measurements were acquired was determined. For such a purpose we locate the centroid of the bubble and only an area equal to twice the initial bubble diameter was analyzed and only in this region the turbulent parameters were calculated (Fig. 3) [27, 28, 29, 30]. This was done because in the literature is reported that only the eddies near to the bubbles can cause strong deformations onto the bubbles surface [16].
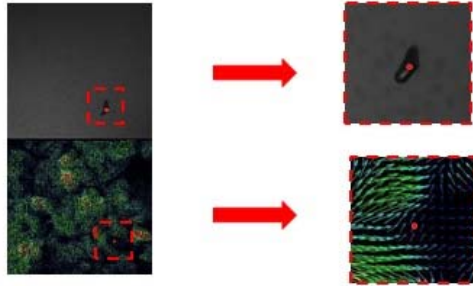

Figure 3.3: Determination of the interesting area over which the analysis was performed.

3.2.3 Analysis of the Image (Image Processing)

The deforming process was recording by means of a high speed video camera (Phantom SpeedSense 9040) with a resolution of 1632×1200 square pixels. The bubble aspect ratio was used to quantify the degree of surface deformation of bubbles [31], and was taken as the ratio between the major and minor axes of the bubble $\chi = d_l/d_s$ (Fig. 4). When the bubble is spherical this parameter is one and as the bubble is most distorted this value increases. Also we calculate the equivalent diameter as:

$$D_{eq} = \sqrt[3]{d_l^2 \cdot d_s}; \tag{3.1}$$

D_{eq}	χ	Re_b	We_b
mm	[−]	[−]	[−]
3.1	1.97	884.3	3.38

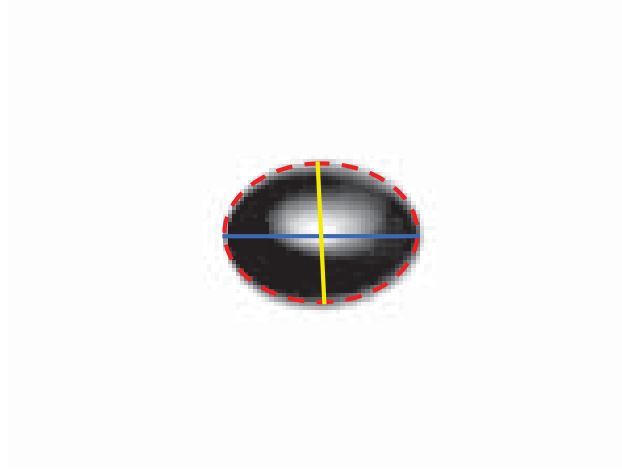Experimental determination of bubble parameters.

Figure 3.4: The image shows a typical measurement of the major (blue line) and minor (yellow line) axes of the bubble.

where d_l and d_s are the large and short axis of the bubble detected in the two dimensional image. The bubble parameters are depicted in Table 3.2. An important parameter to take into account is the Reynolds-Taylor number to quantify the ratio of the turbulent intensity of eddies in the region of interest that direct will affect the bubbles. This parameter is based on the Taylor scale and the fluctuating velocities to quantify the turbulence intensity. Other parameter to be considered is the turbulent Weber number which relates the inertial effects of the fluctuating velocities over a bubble and the superficial forces:

$$Re_\lambda = \frac{u'_{rms}(d)\ \lambda}{\nu};$$ (3.2)

$$We_t = \frac{\rho\ u^2(d)\ D_e}{\sigma};$$ (3.3)

where ρ, σ, μ and ν are the density, surface tension and dynamic and kinematic viscosity of the continuous phase. The working fluids used in this study were tap water and air. The velocity $u(d)$, is the fluctuating velocity measured in a section around the bubble with a size corresponding at two times the initial equivalent bubble diameter as we describe previously.

3.3   Results

In Figs. 3.5 and 3.6, we can observe the deformation process of bubbles of equal size as a function of the time, for two different cases, when the bubble breaks up

and when this does not occur, respectively. In Fig. 3.7 Re_λ was calculated at every instant of the bubble deformation process. Observing the aspect ratio change in time in Fig. 3.7a, which corresponds to the case when the bubble does not breaks up the deformation ratio reach large values but the Re_λ at each instant is not large enough to produce the rupture. Comparing this results with Fig. 3.7b shows the change of the aspect ratio as function of the time the increment of the χ is gradual; however, when the bubble breakup occurs the deformation is caused by a sudden change of the velocity fluctuation represented in the Reynolds-Taylor number values even if the values of deformation are smaller. Moreover we can examine that when an abrupt change in the Re_λ takes place, the deformation changes substantially. This allow us to appreciate the bubble response to the large gradients of the fluctuating velocities which can be directly responsible of the breakup (Fig. 3.5), in contrast to what was previously recognized, as the resonant mechanism [16].

In Fig. 3.8 the modification of the We_t as a function of the time is presented. For each instant the bubble deformation ratio was calculated. For the different instants when the bubble breaks up is not observed (Fig. 3.8a), we can notice an oscillation or balance among the forces that acts over the bubble surface, since the deformation is controlled by the balance of the superficial tension forces and the inertial ones. In that way a change in the natural frequency over the bubble surface is induced and the initial balance is lost and the bubble changes it shape. The bubble behavior is similar for the instances when breakup is observed (Fig. 3.8b), but we can discern an increase in the turbulent Weber number. It is interesting to note that in the highest peak of the plot at the largest value of We_t the deformation does not increase, but in the second peak the a high We_t is follow by the an important deformation and change in the aspect ratio. Now a question remains unanswered: why the bubbles do not breakup for the large values of We_t if the deformation increases? We can infer that this occurs when the bubble deformation is not fast enough; however, in the case of the bubble breakup the deformation increase. This can be explained in terms of the intermittency of the fluctuating velocities when the bubble deformation increase and diminish. This cannot be identified if we only take into account the increase of the root mean square values.

3.4 Conclusions

From the images sequences obtained in this work, we can recognize that breakup forms small bubbles of unequal sizes. From the velocimetry results it can be argued that the presence of large fluctuating velocity gradients around the bubbles will be responsible for the breakup. However, a difference exist in the transport of moment in the interface gas-liquid which causes some zones in the bubble surface to be accelerated, which can lead to breakup. This behavior results from the intermittent fluid motion in the vicinity of the bubble, as indicated by the measurements. From the analysis of the bubble-turbulence interaction we can conclude that there exist fluctuations of pressure inside the bubbles. It is evident that there is a competition among the forces that dominate the process, namely the superficial tension and the
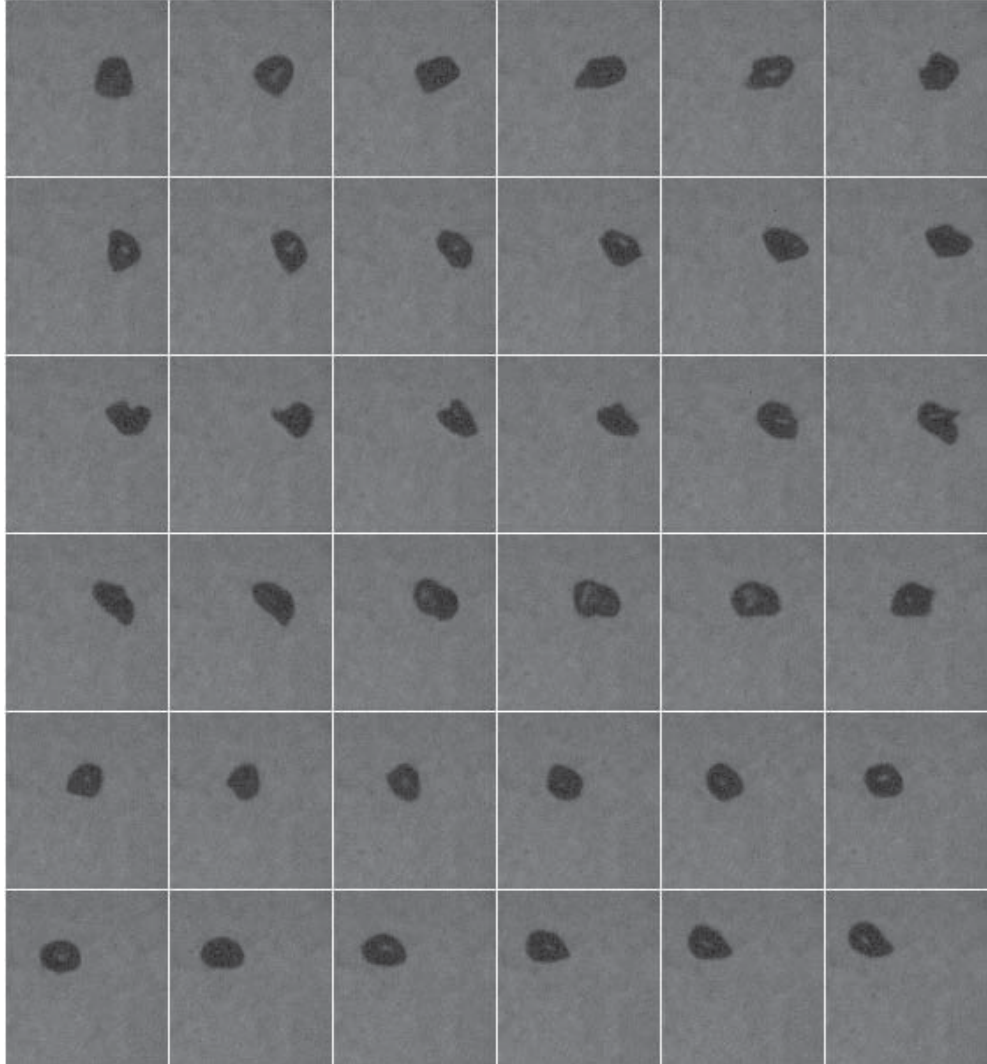
Figure 3.5: Bubble deformation process, the images sequence was taken at 500 Hz. No-bubble breakup case, the bubble size is 3.1 mm.
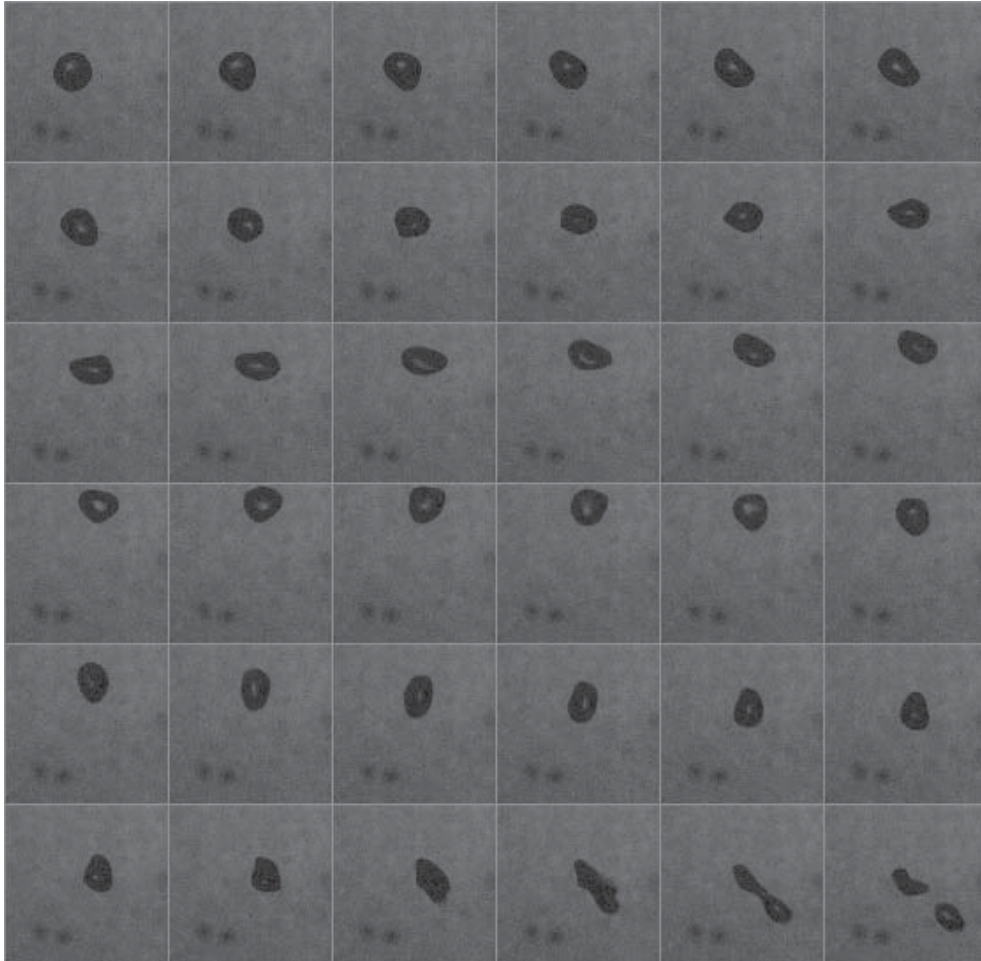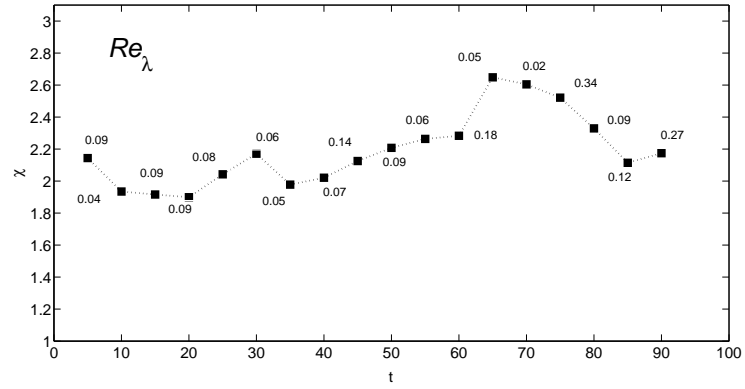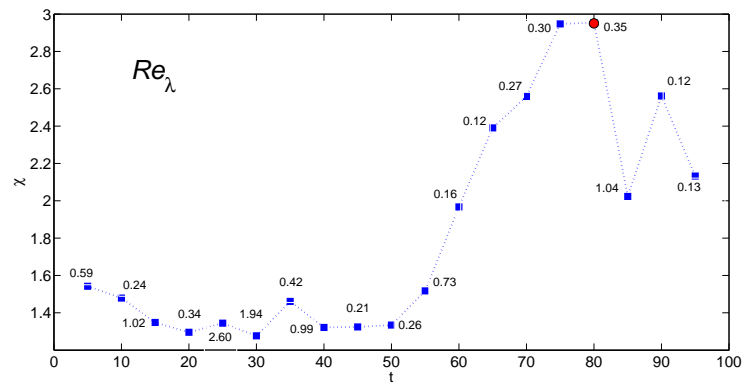
Figure 3.6: Bubble deformation process, the images sequence was taken at 500 Hz. Bubble breakup case, the bubble size is 3.0 mm.
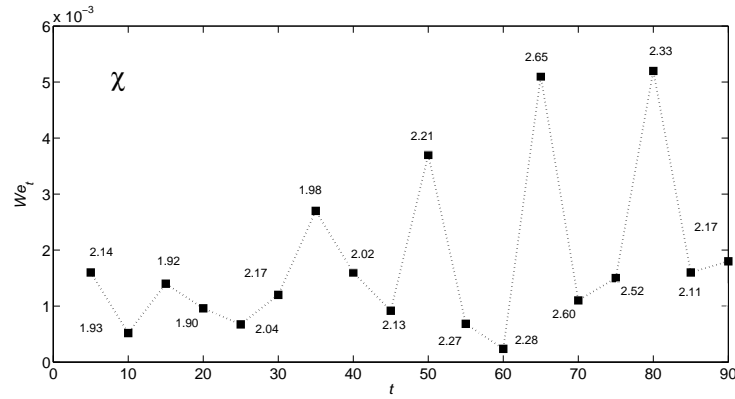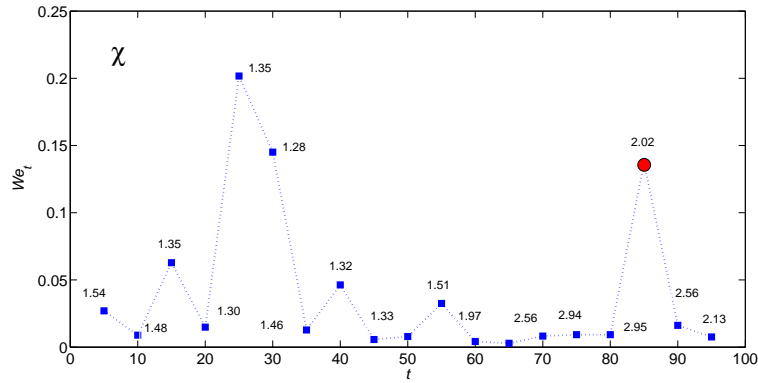
(a)

(b)

Figure 3.7: The aspect ratio as a function of the time is presented for the two cases found a) No-breakup case, b) Breakup case. At each instant the Re_λ was calculated the red dot shows the instant when the bubble breaks up.

Figure 3.8: The turbulent Weber number (We_t) as a function of the time is presented for the two cases found a) No-breakup case, b) Breakup case. At each instant the deformation ratio χ was calculated the red dot shows the instant when the bubble breaks up.

inertial forces. The intermittent behavior of the velocity components contribute to the eventual breakup of bubbles, when the surface tension force is not able to retain the bubble shape and the bubble surface does not follow the fast movements of the fluid elements around of it. In the same manner we can suppose that there exist a mechanism of flow redistribution which produce the breakup when the bubbles try to recover their original shape.

Bibliography

[1] J. Dunkel, S. Heidenreich, K. Drescher, H. H. Wensink, M. Bar, and R. E. Goldstein, Fluid dynamics of bacterial turbulence, Phys. Rev. Lett. 110, 228102,(2013).

[2] A. Brandenburg and A. Nordlund, Astrophysical turbulence modeling, Rep. Prog. Phys. 74, 046901 (2011).

[3] S. Elghobashi and G. C. Truesdell, On the two-way interaction between homogeneous turbulence and dispersed solid particles. I: Turbulence modification, Physics of Fluids A: Fluid Dynamics 5, 1790 (1993).

[4] S. Elghobashi, On predicting particle-laden turbulent flows, Applied Scientific Research 52, 309 (1994).

[5] L. F. Richardson, Weather prediction by numerical process (Cambridge University Press, UK, 1922).

[6] Tatterson, G. B. Fluid Mixing and Gas Dispersion in Agitated Tanks, Mc Graw-Hill, Inc. 1991.

[7] Mancilla E., Soto E., Yatomi R., Ascanio G., Zenit R., Hydrodynamic Characterization of Three Axial Impellers under Gassed and Ungassed Conditions, Submitted to Industrial & Engineering Chemical Research, 2014.

[8] Birouk M., Chauveau C., Sarh B., Quigards A., Gkalp I., Turbulence Effects on the Vaporization of Monocomponen Single Droplets, Combustion Science of Technology , 413-428, 113-114, 1996.

[9] Fernando H. J. S. and De Silva P. D., Note on Secondary Flows in Oscillating-Grid, Mixing-Box Experiments, Physics of Fluids 1849-1851, 5, 1993.

[10] Krawcynski J. F., Renou B., Danaila L., Small-scale Measurements in a Partially Stirred Reactor, Experiments in Fluids 40, 667-682, 2006.

[11] Villermaux E., Hopfinger E., Periodically Arranged Co-Flowing Jets, Journal of Fluid Mechanics, 63-92, 263, 1994.

[12] Wang S. J., Mujumdar A. S., Flow and Mixing Characteristics of Multiple and Multi-set Opposing Jets, Chemical Engineering and Processing, 703-712, 46, 2007.

[13] Legendre D., Magnaudet J., The Viscous Drag Force on a Spherical Bubble with a Time-Dependent Radius, Physics of Fluids, 550-554,10, 1994.

[14] Legendre D., Magnaudet J.,The lift Force on a Spherical Bubble in a Viscous Linear Shear Flow,Journal of Fluid Mechanics,81-126,368,1998.

[15] Magnaudet J., Eames I., The Motion of High-Reynolds-Number Bubbles in Inhomogeneous Flows, Annual Review of Fluid Mechanics, 659-708, 32, 2000.

[16] Risso F., Fabre J., Oscillations and Breakup of a Bubble Immersed in a Turbulent Field, Journal of Fluid Mechanics, 323-355, 372, 1998.

[17] Sleicher C. A., Jr., Maximum Stable Drop Size in Turbulent Flow, American Institute of Chemical Engineers Journal, 8, 471-477, 1962.

[18] Collins S. B., Knudsen J. G., Drop-size Distributions Produced by a Turbulent Flow of Immiscible Liquids, American Institute of Chemical Engineers Journal, 16, 1072-1080, 1970.

[19] Walter J. F., Blanch H. W., Bubble break-up in gas-liquid Bioreactors: Breakup in Turbulent Flows, The Chemical Engineering Journal, 32, B7B17, 1986.

[20] Hesketh R. P., Etchells A. W., Russel T. W. F., Bubble Breakage in a Pipeline Flow, Chemical Engineering Science, 46, 1-9, 1991.

[21] Mancilla E., Zenit R., Ascanio G., Soto E., Bubbles in Isotropic Homogeneous Turbulence, Fluid Dynamics in Physics, Engineering and Environmental Applications, Environmental Science and Engineering, Springer Berlin Heidelberg, 529-530, 2013.

[22] Hinze J. Turbulence, McGraw-Hill, New York, 1975.

[23] Birouk M., Sarh B., Gkalp I., An Attempt to Realize Experimental Isotropic Turbulence at Low Reynolds Number, Flow, Turbulence and Combustion, 325-348, 70, 2003.

[24] Hwang W, Eaton J. K., Creating Homogeneous and Isotropic Turbulence without Mean Flow, Experiments in Fluids, 444-454, 36, 2004.

[25] Mancilla E., Martínez-Ortíz M., Hernández-Díaz D.,Méndez-Díaz S., Zenit R. Looking for Isotropic Turbulence: A New Experimental Device, To be submitted to Experiments in Fluids.

[26] Mancilla E., Caracterización de un flujo turbulento en la producción de una emulsin. Master Thesis, UNAM, 2009.

[27] Adrian R. J., Christensen K. T., Liu Z. C., Analysis and Interpretation of Instantaneous Turbulent Velocity Fields, Experiments in Fluids, 275-290, 29, 2000.

[28] Saarenrinne P., Piirto M., Turbulent Kinetic Energy Dissipation Rate Estimation from PIV Velocity Vector Fields, Experiments in Fluids, Supplement 1, 300-307, 29, 2000.

[29] Sheng J., Meng H., Fox RO., A Large Eddy PIV Method for Turbulence Dissipation Rate Estimation, Chemical Engineering Science, 4423-4434, 55, 2000.

[30] Martínez-Bazán C., Montaés J. L., Lasheras J. C., On the breakup of an air bubble injected into a fully developed turbulent flow. Part 1. Breakup frequency, Journal of Fluid Mechanics, 401, 157-182, 1999.

[31] Martínez-Mercado J., Palacios-Morales C.A., and Zenit R.,Measurement of pseudoturbulence intensity in monodispersed bubbly liquids for 10<Re<500, Physics of Fluids, 103302-103302-13 , 19, 2007.

Chapter 4

Summary and General Conclusions

Turbulent flows carrying different types of particles can be found everywhere. Diverse examples both in industrial applications and in nature can be identified. Their relevance is notorious in every day life. Particles can be lighter or heavier that the carrier fluid. The case analyzed in this work is the first one. The knowledge of the interactions of the turbulent flow field and the bubbles is important to improve mass and heat transfer, and the overall mixing in industrial devices. This thesis deals with bubbly-turbulent flows mainly in two different flow conditions. Bubbles in anisotropic turbulence and bubbles in a controlled nearly isotropic turbulent environment.

In the first chapter, we experimentally study the flow and the mixing performance induced by three different axial impellers in turbulent conditions in gassed and ungassed circumstances. The results show a slight reduction in power consumption for the three impellers in the turbulent regime when comparing it with the single phase cases. Using the Particle Image Velocimetry (PIV) technique we determined the characteristic flow patterns generated by the three agitators under gassed and ungassed conditions. The single-phase flows for each agitator are clearly defined by the formation of several recirculation zones around the tip impellers and up to bottom circulation zones. We recognize an extreme change in the flow patterns when we add a disperse phase into the tank. This was observed particularly for conventional impellers (Intermig and PBTD). This pattern variation reveals that turbulent impellers are not capable to manage the gas flow rates used in this thesis. Is important to notice that under the different conditions used in this research, the Maxblend impeller showed the best performance even if its main flow pattern is modified (switching from axial to radial). This impeller is able to handle more gas that the other ones and conserves a strong liquid flow in the whole tank area. In the turbulence distribution study of the Intermig and the PBTD impellers compared with the Maxblend impeller we found that for the conventional agitators the turbulent intensity are far from homogeneous but in the case of the Maxblend impeller this produces a large and homogeneous region covering almost

61

the complete vessel. When we analyzed the turbulent intensity magnitude we can identify the presence of higher values for the Maxblend impeller in large regions comparing with the performance of the turbulent agitators. The different performance can be explained in terms of the diverse geometries of the impellers and due to the different gas injection device used in this work.

The experiments presented in the second chapter were performed in the Physics of Fluids Group of the University of Twente in the Netherlands. In this section, we focused on the influence of bubbles over a controlled turbulent environment. For this purpose we used a device built with this objective (Twente Water Tunnel). To carry out the analysis we use a previously defined quantity called the bubblance parameter which is defined as the ratio between the turbulence induced by bubbles to the turbulent intensity in the mean flow. Using this ratio we can compare and analyze which are the relevant criteria that can lead to an enhancement or reduction of the turbulence intensity and which are the physical parameters underlying such interaction. For this objective we methodically varied the bubblance parameter since a large range, from the pseudoturbulence regime (b $= \infty$) to the single phase turbulence (b $= 0$), passing over different intermediate values, modifying the gas fraction. To achieve a complete characterization of the turbulent flow field it was necessary to use a technique with full temporal and spatial resolution. For this purpose we used the phase-sensitive constant-temperature anemometry (CTA). This is an excellent technique to discriminate the bubble's collisions form the flow signal. From the data captured in this way, we obtained the fluctuating velocities of the flow induced by the interaction of the bubbles with the turbulent media. In this experiment we injected into the flow two different bubbles sizes (2-4, 3-5mm). From the analysis of the bubble velocity probability density functions (PDFs) and liquid energy spectrum for the different cases under study ($\alpha =0$ to 2%) we found that PDFs for the liquid velocity fluctuations in the bubbly systems (b > 0) exhibits an asymmetric behavior and a more pronounced fluctuations in relation with the Gaussian profile (characteristic of the isotropic turbulence). With the increase of the liquid turbulent intensity (b < 1), the PDFs manifest a weak dependence with b parameter. This non-Gaussian response can be attributed to the clustering formation, which will modify the overall flow structure. In the energy spectrum analysis, it had be noted that for the two different experimental setups (two different bubble sizes and varying the b parameter) the energy spectrum scaling follows the Kolmogorov law (-5/3 slope) for the small frequencies, corresponding to the large scales. But in the inertial subrange exist an enhancement of the wake decay and all the spectra shows a -3 conduct. This results can be interpreted as that the life time of the bubble's wakes are larger that the smallest turbulent eddies. This behavior does not show any dependence with the bubblance parameter. Also this can be associated to the spatial distributions mentioned before mainly due to the clustering formation.

In the last part of this thesis, we study the deformation process of a single bubble in homogeneous isotropic turbulence. The turbulent flow was generated by means of controlled water jets pointing out to the center of a chamber. The turbulent characterization was obtained using the Particle Image Velocimetry technique

(PIV). We obtain a nearly homogeneous isotropic turbulent flow controlling the velocity injection of the water to allows us to obtain large turbulent intensities at a low Re_λ. Two main modes were observed, when the bubble breakage is present and when this does not occur. From the examination of the bubbles deformations and the velocity profiles we observed the appearance of large velocity fluctuation gradients in the vicinity of the bubbles surface that will guide to the breakup due to the intermittent nature of the flow. We can observe that this behavior is not recognizable if we only take into account the increment in the turbulent intensity. In addition, it is evident from our measurements that the difference in transport moment in the gas-liquid interface is important, showing us that the bubbles surfaces had a different response time scale than the flow and some zones of the surface are accelerated leading to the breakage process. We can conclude that large fluctuations in the bubble internal pressure are present and flow redistribution exists. The large gradients of fluctuating velocities around the bubble surface generates and abrupt change in pressure inside the bubble that will leads the bubble breakup.

In all the cases considered in this thesis we deal with interactions between bubbles and a turbulent flow, which can be isotropic or not. In all the cases under analysis the experimental conditions of turbulent intensities are similar and are presented in a wide range. Moreover the bubbles sizes employed in the different sections were of the same order of magnitude (2-4 mm). In the results presented along this work we can find that the bubble-turbulence interactions clearly depends on the amount of gas supplied to the system, owing to this can yield to diverse types of couplings, namely, one-way coupling up to four-way-coupling.

Comparing the results obtained both in the first and second chapters; we can note that when the bubbles are immersed in turbulent media, these are able to modify the transfer rate of power among the scales accelerating the process, which can result in a fast dissipation of the energy flow. Furthermore, as we appreciate in the case of the water tunnel the bubble clustering is important. The same phenomena is present in the stirred tanks in the zones near to the impellers, which has been corroborated in the past. This could be a considerable factor to explain the diminishing of the turbulence levels in the two-phase mixing vessels, in which the turbulent decay is evident. In the zones far away from the agitators in which the cumulus are not present, we can talk of a oneway coupling phenomena that is studied in the last section. In the chapter three we consider situations in which the bubbles are affected by turbulent stresses and the breakage is possible. But in the arrangements employed in the other chapters (one and two), there exits several aspects that will change this breakage process, this could be owing to the difference in the flow conditions (isotropy, anisotropy), geometry (water channel, stirred vessel) and bubbles presents into the flow (gas fraction, clustering), and the individual interaction of the bubble surface and the fast velocity fluctuations are not observed.

We can conclude from previously mentioned, that if actually, the characterization and comparison of such systems is complicated due to the complex flows investigated and the diverse experimental conditions tested, this work can be used as a basis to understand the phenomena associated to these interactions and pro-

vide the knowledge of the predominant factors which play an important role in each one of the situations.